Ratio-based sensing of two transcription factors regulates the transit to cell differentiation

Authors:

Sebastian M. Bernasek*[,1], Suzy SJ Hur[*,2], Nicolás Peláez[*,1,3,4,10], Jean-François Boisclair Lachance[2], Rachel Bakker[3], Heliodoro Tejedor Navarro[6], Nicelio Sanchez-Luege[2], Luís A. N. Amaral[1,5,6,7], Neda Bagheri[1,6,7,8,ϒ], Ilaria Rebay[2†], and Richard W. Carthew[3,7,9,†]

[1] Department of Chemical and Biological Engineering, Northwestern University, Evanston, IL.

[2] Ben May Department for Cancer Research, University of Chicago, Chicago, IL.

[3] Department of Molecular Biosciences, Northwestern University, Evanston, IL

[4] Division of Biology and Biological Engineering, California Institute of Technology, Pasadena, CA.

[5] Department of Physics and Astronomy, Northwestern University, Evanston, IL.

[6] Northwestern Institute on Complex Systems, Northwestern University, Evanston, IL.

[7] NSF-Simons Center for Quantitative Biology, Northwestern University, Evanston, IL.

[8] Chemistry of Life Processes, Northwestern University, Evanston, IL.

[9] Department of Biochemistry and Molecular Genetics, Northwestern University, Evanston, IL.

[10] Howard Hughes Medical Institute (HHMI), Hanna H. Gray Fellows Program.

[*] **These authors made equal contributions.**

[ϒ] Current address: Department of Biology, University of Washington, Seattle WA

[†] Corresponding authors (irebay@uchicago.edu; r-carthew@northwestern.edu)

ABSTRACT

Cell state transitions depend on transcription factors to effect mRNA expression changes. Although certain transitions are directed by change in absolute concentration of single transcription factors, transitions in animal cells frequently require combinations of multiple factors. To investigate how cells sense and respond to concentration changes of concurrently expressed factors, we quantified the expression dynamics of the *Drosophila* transcription factor activator-repressor pair Pnt and Yan during photoreceptor differentiation. Progenitor cells maintain a constant ratio of Pnt-to-Yan despite extensive cell-to-cell variation in absolute protein concentrations. A rapid and sustained increase in the ratio accompanies each progenitor cell as it transitions to a photoreceptor state. Perturbations disrupting the ratio result in gains or losses of these transitions. We used biophysical modeling to illustrate how a ratiometric system can produce differential transcription factor binding necessary to drive transitions. Reliance on relative rather than absolute concentration as the control variable may allow ratiometric systems to function more robustly under conditions of component variability.

INTRODUCTION

Organismal development proceeds through a sequence of cell state transitions that yield increasingly tissue-specific cellular states. Cell states and the transitions between them are often modeled as outcomes of a dynamical system. Cell states, typically characterized by their mRNA and protein expression profiles, are regulated by transcriptional activators and repressors that dynamically interact according to certain rules (1). Studies of cell state transitions underlying numerous developmental decisions have identified the relevant transcription factors, elucidated their regulatory relationships and organized them into networks bootstrapped from inferred pairwise interactions. Although network diagrams provide static abstractions of cell state transitions by linking input transcription factors to output mRNA and protein expression, on their own they do not reveal the temporal dynamics or the quantitative rules that drive these decisions.

Notable progress has been made in understanding how unicellular organisms (2) and *in vitro* cultured systems (3) respond to changes in transcription factor concentrations to execute state transitions. These studies provide support for two distinct strategies. In the first, changes in the absolute concentrations of key transcription factors provide ultrasensitive regulation and trigger distinct differentiative cell state transitions (4–7). In the second, state transitions are regulated by relative rather than absolute changes in single transcription factor concentrations (8, 9). Together

these studies provide conceptual insights on how a cell may sense individual transcription factor concentrations and use changes in their levels to regulate the transit toward a particular state.

However, in complex multicellular eukaryotes, cells must sense and integrate the expression dynamics of multiple transcription factors to make accurate cell state decisions. In such contexts it is unknown whether cells use emergent properties such as ratiometric changes in transcription factor levels to execute state transitions. Compounding the difficulty of answering this question, simultaneous measurement of multiple transcription factor levels at single cell resolution, over the time scales needed to follow a cell state transition, still presents a major technical barrier in most multicellular developing tissues.

Unique features of the developing *Drosophila* eye allow us to overcome these challenges. We focused our study on two ETS-family transcription factors, the activator Pointed (Pnt) and the repressor Yan (also known as Anterior Open, or *Aop*), that compete for the same DNA binding sites across the genome (10–20). This activator/repressor pair functions downstream of receptor tyrosine kinase (RTK) signaling to regulate cell state transitions in many developing *Drosophila* tissues, including progenitor to photoreceptor transitions in the eye (10–12, 21–28). During eye development, eight distinct photoreceptor (R) neurons, R1-R8, are specified from a specific pool of multipotent progenitor (P) cells that co-express Pnt and Yan and are poised to differentiate (Figures 1A and S1A) (28). Each P cell to R cell transition, with the exception of the P to R8 transition, requires RTK signaling (29) to resolve the opposing transcriptional inputs from Pnt and Yan on their shared target genes. During these transitions, concomitant downregulation of Yan activity and upregulation of Pnt activity is thought to shift the state of a poised P cell in a pro-differentiation direction toward a young R cell state (Figure 1A) (21–23, 29–31). Other transcription factors combinatorially instruct each transitioning young R cell about which specific R cell type to choose (10, 12, 32, 33).

In this study, we investigated how poised P cells sense and respond to changes in abundance of Pnt and Yan proteins by measuring the expression dynamics of these two transcription factors in thousands of individual nuclei during P to R cell state transitions. We find that P to R cell state transitions are marked by a change in the relative ratio of the Pnt and Yan proteins. P cells maintain

96 a fairly constant ratio of Pnt-to-Yan protein levels over time despite extensive cell-to-cell variation
97 in the absolute protein levels. P cells that initiate transitions to R fates experience a rapidly
98 increasing ratio. As R cells mature, the Pnt-to-Yan ratio remains stably elevated above the ratio of
99 the remaining P cells. Confirming the biological importance of this observation, directed
100 perturbations that artificially change the ratio result in either gain or loss of cell state transitions
101 and defects in tissue patterning. We propose that cells in the developing eye rely on a ratiometric
102 sensing mechanism in which a sustained relative increase in the Pnt-to-Yan ratio initiates and
103 accompanies progenitor to differentiated state transitions.
104
105 **RESULTS**
106
107 **Single cell *in vivo* measurements of activator and repressor transcription factor dynamics**
108 **connect protein abundance and cell states in a developing tissue.**
109 The developing *Drosophila* eye provides a powerful *in vivo* context to causally link transcription
110 factor dynamics to cell states. Each eye contains a pool of ~20,000 undifferentiated progenitor (P)
111 cells from which a subset of ~6,000 transition to photoreceptor (R) cells. Within each eye, the
112 ~6,000 R cells are organized into ~ 750 identical units called ommatidia, each containing the same
113 cohort of eight R cells (R1-R8). R cell differentiation and ommatidial formation begin in the
114 posterior margin of the larval eye, from which point a morphogenetic furrow (MF) sweeps across
115 the tissue with a constant velocity in the anterior direction. A new row of ommatidia forms every
116 ~2 hours in the wake of the moving MF as it transits across the eye (Figures 1B). Within each
117 nascent ommatidium, the eight R cells differentiate from a local pool of P cells in a stereotypic
118 sequence: first R8, then R2 and R5, then R3 and R4, then R1 and R6, and finally R7 (Figure 1B
119 and S1A) (34, 35). Each R cell type can be reliably identified as soon as it becomes
120 morphologically and positionally distinct from the P cell population, which occurs before the onset
121 of detectable neuronal or photoreceptor-specific mRNA or protein expression (31). Remaining P
122 cells that do not transition to any of the R cell types during this period differentiate into other
123 ommatidial cell types at later stages. Together, all these features make it possible to follow the
124 temporal progression of thousands of individual P to R transitions simultaneously in a single fixed
125 tissue sample, allowing quantitative, single cell resolution-examination of the dynamical processes
126 that regulate these transitions.

127

128 To understand how P vs. R cell states are resolved, we measured Pnt and Yan levels simultaneously
129 in thousands of individual cell nuclei before, during, and after P to R transitions. Pnt levels were
130 measured using a functional GFP-tagged allele (28) while Yan levels were measured indirectly
131 using a monoclonal antibody that we had previously shown to be calibratable (31). We adapted
132 our previous approach (31) to convert the spatial position of each cell to a specific developmental
133 time. Given that the MF moves at constant velocity across the developing eye (36), we converted
134 the spatial position of the MF to developmental time $t = 0$, with each successive row of ommatidia
135 posterior to the MF marking successive 2 h intervals. Individual P and R cell types were identified
136 using their stereotyped morphology and the apical-basal position of their nuclei (Figure S1). Cross-
137 validation with cell type-specific markers showed our identification approach has an estimated >97%
138 accuracy for all P and R cell types (Table S1), matching our previous study (31). We refer to the
139 earliest identifiable cells within each R cell differentiation trajectory as "young" R cells and the
140 neighboring poised P cells from which they diverge as "concurrent" P cells. Although our approach
141 cannot measure the protein dynamics of an individual P cell transitioning to a specific R state in
142 real time, quantifying protein expression in hundreds to thousands of spatially ordered cells of
143 defined identities along the temporal trajectory provides a macroscopic view of dynamics from
144 which mechanistic principles can be extracted.

145

146 **Pnt and Yan expression pulses coincide with critical windows of P to R cell state transitions.**
147 We first measured Pnt and Yan expression dynamics in the P cell population (Figure 1C-E). In this
148 population, average expression levels of both Pnt and Yan increased immediately prior to the
149 initiation of R cell differentiation, reached maximal expression, and then slowly decayed. Pnt
150 expression peaked twice in P cells whereas Yan expression peaked once, in between the two Pnt
151 expression peaks. Despite their alternating maximal amplitudes, the overall induction and decay
152 of Pnt and Yan proteins were concurrent in P cells (Figure S2), consistent with our previous
153 qualitative observations (Lachance et al., 2014).

154

155 The first and second peaks of Pnt protein expression in P cells coincided with the two successive
156 waves of R cell differentiation (Figure 1C,F,H) (30). P cell transitions to R8, R2/R5, and R3/R4
157 occurred during the first Pnt peak (Figure 1C,F), while transitions to R1/R6, and R7 occurred

158 during the second peak (Figure 1C,H). All young R cells at these transition windows displayed a
159 25-50% increase in Pnt levels, which decayed as these cells matured over time. Yan showed the
160 opposite dynamical behavior during R cell differentiation; young R cells exhibited lower Yan
161 protein levels compared to concurrent P cells (Figure 1G,I). Yan levels rapidly decayed in
162 maturing R cells, reaching a basal level that was at least two-fold lower than that in concurrent P
163 cells. To summarize, pulses of the activator Pnt and the repressor Yan coincide with two windows
164 of P to R cell state transitions. Within these windows, a respective increase and decrease in Pnt
165 and Yan protein levels accompany the transitions.
166
167 **P to R state transitions are robust to variation in Pnt and Yan protein levels.**
168 We previously found that P to R state transitions are robust to systematic perturbation of absolute
169 Yan protein levels (22, 31). Could cell state transitions be similarly robust to changes in Pnt protein
170 levels? To answer this question, we decreased Pnt protein levels by reducing the *pnt* gene copy
171 number from two (wildtype) to one. As expected, having a single copy of the *pnt* gene resulted in
172 a ~ 50% reduction in Pnt protein levels compared to levels measured in animals with two copies
173 (Figure 2A,C). Pnt levels were not only reduced in P cells, but when R cells differentiated from
174 single-copy *pnt* P cells, there was a corresponding reduction in the maximal amplitude of Pnt levels
175 reached by these cells (Figure 2A,C). Notably, P to R state transitions were robust to this
176 significant reduction in Pnt protein levels, and eyes developed with a wildtype pattern and
177 morphology (Figure S3).
178
179 Unexpectedly, when we measured Yan levels in P cells in these single-copy *pnt* eyes, we found
180 that Yan protein levels were significantly reduced, despite these cells still having two copies of the
181 *yan* gene (Figure 2B,D). This suggests a role for Pnt in positively regulating Yan expression, and
182 perhaps a mechanism of coordinated regulation of Pnt and Yan abundance. The qualitatively
183 parallel behaviors of Pnt and Yan in this experiment prompted us to quantitatively assess the extent
184 to which Pnt and Yan levels are coordinated within individual nuclei. To do this, we calculated the
185 Pnt-to-Yan ratio in individual P cells at each P-to-R transition point and compared the results
186 between populations with one vs. two copies of the *pnt* gene. Consistent across the different
187 transition points, the Pnt-to-Yan ratios in single copy *pnt* P cells were remarkably similar to the
188 ratios in two-copy *pnt* P cells (Figure 2E).

189

190 **A reset in the Pnt-to-Yan ratio coincides with P to R cell state transitions.**

191 Given that the robustness of cell state transitions to systematic variation in *pnt* gene copy number
192 was accompanied by a stabilized Pnt-to-Yan ratio in P cells, we wondered if the ratio might act as
193 a control parameter regulating the transitions from P to R states. Consistent with this possibility,
194 the average Pnt-to-Yan ratio in P cells remained dynamically stable about a fixed value over time
195 (Figure 3A). Greater cell-to-cell fluctuations in the ratio coincided with the specific times when
196 Pnt and Yan levels peaked (Figures 3A and 1D,E).

197

198 We next asked whether the Pnt-to-Yan ratio was also invariant in R cells over time. We first
199 examined the ratio in R7 cells along their differentiation trajectory. Strikingly, the average Pnt-to-
200 Yan ratio was higher in young R7 cells relative to their concurrent P cells (Figure 3A, note log
201 scale of y-axis). The ratio rose and then gradually fell as R7 cell differentiation progressed over
202 time, but always remained at higher values than that of concurrent P cells. Examination of the Pnt-
203 to-Yan ratio dynamics in all other R cell types revealed a similar and consistent rapid increase as
204 R cells differentiated from the P cell pool, followed by a gradual decline to a new steady value that
205 was higher than that of concurrent P cells (Figure S4).

206

207 The stable Pnt-to-Yan ratio in P cells rapidly shifts to a new, higher ratio value as P cells transition
208 to become R cells, and subsequently stabilizes at that higher value in the R cells. This observation
209 prompted us to hypothesize that the ratio becomes destabilized during state transitions and then
210 re-set as cells stabilize their states. If so, then cell-to-cell heterogeneity of this ratio should rise
211 during the time-windows for state transitions, and then subside as cell states are resolved. We used
212 our established method (31) to quantify cell-to-cell heterogeneity of Pnt levels, Yan levels, and the
213 ratio along each P to R differentiation trajectory (Figure S5). We found increased heterogeneity in
214 the ratio, as quantified by the coefficient of variation, coincided with the time windows in which
215 subsets of P cells differentiated to R cells. The enhanced heterogeneity persisted in young R cells
216 and diminished as they matured.

217

218 We next focused on how ratio values are distributed in young R vs. concurrent P cells at the time
219 windows of cell state transitions. Interestingly, we found that there was a substantial overlap in

220 ratio values between young R cells and concurrent P cells in these time windows. Nevertheless,
221 the Pnt-to-Yan ratios of most young R cells were greater than the median ratio for the concurrent
222 P cells (Figure 3B-F). This resulted in a significantly higher average ratio in all young R cell types
223 relative to their concurrent P cell neighbors (Figure 3G, $P<0.001$, KS 2-sample test). Together
224 these measurements reveal that a subset of P cells transiently elevate their Pnt-to-Yan ratio at the
225 P-to-R state decision points, but that only young R cells maintain the elevated ratio as they mature.
226

227 **Controlled perturbations of the Pnt-to-Yan ratio bias P cells towards or against R state**
228 **transitions.**

229 If the Pnt-to-Yan ratio is a control variable that triggers P to R state transitions, then tuning up or
230 down the proportion of P cells that stably elevate the ratio should correspondingly change the
231 proportion of cells that transition to R states. As a first test of this hypothesis, we altered the RTK
232 signaling circuitry to artificially induce a ratio increase in a larger number of P cells at specific cell
233 state transition time-windows. We expressed a Ras^{V12} transgene encoding a constitutively active
234 version of the Ras GTPase under the control of the enhancer/promoter of the *sevenless* (*sev*) gene.
235 This induced transient expression of Ras^{V12} in subsets of P cells during the R3/R4 and R7 transition
236 points, and then stable expression in mature R3/R4 and R7 cells (Figures 4 and S6) (22, 37, 38).
237 By overriding the endogenous RTK circuitry, this perturbation should increase Pnt protein
238 abundance (Figure 4A). As predicted, *sev>*Ras^{V12} dramatically increased the amplitude and
239 duration of the second peak of Pnt expression in P cells, which coincides with the second wave of
240 R cell differentiation events (Figure 4B). Yan protein levels were weakly reduced in P cells during
241 this time window (Figure 4D). The result was a sustained elevation in the Pnt-to-Yan ratio in a
242 larger number of P cells at the transition window and continuing thereafter (Figure 4C). *sev>*Ras^{V12}
243 expression also resulted in supernumerary R cells that had comparable ratios to neighboring R7
244 cells (Figure 4E). These ectopic R cells were typically found flanking the R7 cell of each
245 ommatidium (Figure S7A,B). Thus, forcing P cells to have an elevated Pnt-to-Yan ratio results in
246 too many P cells becoming R cells, consistent with the ratio being a key control variable that
247 regulates P to R state transitions.
248

249 To further test this hypothesis, we performed the converse experiment by preventing the Pnt-to-
250 Yan ratio from increasing in P cells during transition windows. We used the same *sev*

251 enhancer/promoter to drive expression of a constitutively active form of Yan, Yan^{Act}, which results
252 in accumulation of the repressor protein in the nuclei of R3/4 and R7 cells (Figure 5A) (22, 39)).
253 As expected, R8, R2/R5 and R1/R6 state transitions appeared normal and exhibited normal ratio
254 dynamics (Figures 5E and S8A-D,G,H). There was a mild increase in Yan levels and a delayed
255 increase in the Pnt-to-Yan ratio in young R3/R4 cells (Figures S8E,F). As these cells matured,
256 their ratios reached a steady state value that was comparable to wildtype R3/4 cells.
257
258 In contrast, the *sev>Yan*^{ACT} perturbation resulted in a large reduction in the total number of R7
259 cells (Figure 5B-E). The few cells that could be plausibly identified as R7s were mostly young R7
260 cells. These young R7 cells had diminished Pnt-to-Yan ratios that were comparable to the ratio in
261 concurrent P cells (Figure 5C,D). Comparison of Yan and Pnt expression confirmed that the
262 reduced ratio in these young R7 cells was driven primarily by increased Yan levels (Figure S9).
263 Identifying mature R cells in the adult retina revealed an almost complete loss of R7s (Figures 5E
264 and S7A,C), firmly connecting the failed state transition to the inability of *Yan*^{ACT} expressing P
265 cells to elevate the Pnt-to-Yan ratio.
266
267
268 **Thermodynamic equilibrium modeling of transcription factor competition for DNA binding**
269 **suggests tuning the activator-to-repressor ratio can produce accurate control of**
270 **transcriptional outputs.**
271 How could cells robustly regulate transcription of genes in response to the relative ratio of a
272 transcriptional activator such as Pnt and repressor such as Yan? Since both Pnt and Yan are ETS
273 family transcription factors with overlapping sequence specificity for DNA binding (10–16) the
274 underlying mechanism should reflect competition for binding sites in target gene promoters and
275 enhancers. Because measuring enhancer occupancy at single cell resolution *in vivo* is not yet
276 experimentally feasible, we instead investigated this mechanism *in silico*. We created a
277 mathematical model of the dependence of binding occupancy on the concentrations of a pair of
278 transcription factors that compete for common DNA binding sites. If the activator and repressor
279 compete for occupancy with the same binding affinity, and binding sites are saturated, then
280 equilibrium occupancy by either factor will be more sensitive to the relative concentration of the
281 two factors than to the absolute concentration of both species (Figure S10; see Methods).

However, the situation with Pnt and Yan is more complex. While there are several well-documented target genes that contain enhancers with common binding sites for Pnt and Yan (10–12), Yan binds these sequences with higher affinity than Pnt (12). Moreover, recent experiments suggest Yan and Pnt differentially interpret the structural syntax of cis-regulatory modules (19). This complex phenomenon is a consequence of cooperative interactions between DNA-bound Yan molecules. Specifically, Yan monomers are able to self-associate via their sterile alpha motifs (SAM), enabling DNA-bound Yan monomers to stabilize the recruitment of additional Yan monomers to adjacent sites (19, 40). Because Pnt does not self-associate (41, 42), Yan-Yan cooperativity will bias the activator vs. repressor competition for binding sites.

To evaluate this possibility, we adapted a modeling framework developed to probe the effects of *cis*-regulatory syntax on Yan binding site occupancy (43). The model considers an ensemble of microstates, each defined by a unique configuration of vacant or Yan-bound sites. Each microstate is assigned a thermodynamic potential based on the cumulative influence of strong sequence-specific binding to consensus ETS sites, weak non-specific DNA binding, and SAM-SAM polymerization. We generalized the Hope et al. model by incorporating Pnt as a second transcription factor that competes for occupancy of the same binding sites but does not self-associate (Figure S11A,B). Using this model, we explored how Yan-Yan cooperativity might impact Pnt binding site occupancy to changes in the activator-to-repressor ratio at the enhancer.

We first considered a scenario in which neither Yan nor Pnt exhibit cooperativity (Figure 6A). In the absence of stabilizing SAM-SAM interactions, the landscape of overall binding site occupancy was identical to that obtained with the simple binding model described above (Figures 6A and S11). Increasing the Pnt-to-Yan ratio resulted in a gradual increase in Pnt occupancy for all individual binding sites, producing a titration contour closely resembling a Michaelian curve (Figures 6C and S11C).

Introducing stabilizing SAM-SAM interactions for Yan dramatically sharpened the transition from Yan to Pnt occupancy dominance (Figure 6B). Weighting the energetic contributions of binding strength and polymerization by the statistical frequency of each microstate revealed that the

transition was driven by an abrupt change in the dominant binding mechanism. Polymerization-associated cooperativity effects dominate binding site occupancy when the Pnt-to-Yan ratio is low, while binding strength dominates when the ratio is high (Figure S11D).

Increasing the Pnt-to-Yan ratio revealed nonlinear transitions from low to high Pnt occupancy for each individual binding site (Figures 6C and S11E). These transitions resembled Hill function forms, with sharp thresholds delimiting distinct transcriptional outputs. At low activator-to-repressor ratios, Yan occupancy dominated, while at some critical ratio, Pnt-bound molecules prevented Yan-Yan interactions, ultimately allowing Pnt to outcompete Yan as the ratio increased further. If transcription factor levels are sufficient to saturate binding sites, then relative occupancy by Pnt and Yan should be agnostic to changes in the absolute abundance of either factor, as long as the ratio remains constant.

Because the model was designed to complement rather than recapitulate our *in vivo* measurements of transcription factor expression dynamics, its predictions about molecular mechanism can only provide guidance on how to interpret the experimental data. For example, our comparisons of the Pnt-to-Yan ratio in young R cells relative to the concurrent P cell population (Figures 3B-F) can be viewed as parallel representations to the phase spaces calculated in the model (Figures 6B). Above a certain activator-to-repressor ratio, cells will transition to a new state, while below that threshold, they will remain in the initial state, regardless of the absolute transcription factor concentrations (Figures 6D,E). In this way, small changes in the relative ratio of Pnt-to-Yan would drive cell state changes by eliciting large changes in DNA binding site occupancy, while large changes in absolute Pnt and Yan levels would have little effect so long as the relative ratio remains constant.

DISCUSSION

Our study has quantitatively analyzed *in vivo* a series of cell state transitions that are controlled by the abundance ratio between an activator transcription factor and a repressor transcription factor. In this multicellular developing system, cells in the progenitor pool (P cells) maintain a dynamically constant Pnt-to-Yan ratio necessary to sustain the undifferentiated state. RTK signaling changes the ratio set-point and produces a sustained increase in the ratio, at the same

344 time as it is driving a P cell's transition to differentiation. In this way the relative ratio would
345 directly control the makeup of transcription factor complexes on target genes required for R cell
346 fates, with low Pnt-to-Yan ratios favoring transcriptional repression of target genes and high ratios
347 favoring their transcriptional activation. We support this description with *in vivo* experiments in
348 which we show that the changes in ratio associated with correct cell differentiation can take place
349 at different absolute concentrations of the transcription factors. Indeed, our experiments
350 demonstrate that the Pnt/Yan system is able to maintain a fixed ratio and to make correct transitions
351 over at least a four-fold range of activator and repressor abundance.
352
353 Several features of the Pnt/Yan system may reflect general requirements for any ratiometric-based
354 control mechanisms. First, the regulators must be co-expressed, compete for the same molecular
355 partners and exert opposite effects on them. In eye cells, Pnt and Yan compete for the same DNA
356 binding sites to respectively activate and repress target gene transcription. Second, distinct states
357 must be mechanistically associated with specific ratio values. In our case, a lower activator-to-
358 repressor ratio connects repressor-dominated DNA occupancy to maintenance of the progenitor
359 state, while a higher ratio couples activator-dominated occupancy to differentiation. Third, to
360 induce a new state, the initial ratio set-point point must be changed. In our system, the initial set
361 point in P cells is buffered by a compensatory mechanism that keeps the ratio dynamically stable.
362 During the transit to differentiation, RTK signaling increases the ratio, most likely by differentially
363 regulating the synthesis and degradation of Pnt and Yan through a combination of transcriptional
364 and posttranscriptional mechanisms (44). To override the progenitor state ratio set point, signaling
365 must induce changes that are different either in kind and/or in magnitude from those that set the
366 initial ratio. Fourth, for a system to be controlled by molecular ratios rather than by absolute
367 concentrations, its output must rely on the probability of binding of the two transcription factors
368 to common DNA sites or partners, which is dictated by their relative concentrations. Finally,
369 incorporating cooperativity can make a ratiometric system tunable and sensitive to small changes
370 in the ratio.
371
372 *In silico* modeling of a Pnt/Yan-like system suggests that stabilizing interactions between repressor
373 molecules bound to adjacent DNA sites could sensitize enhancer occupancy to the relative
374 abundance of the competing transcription factors. Indeed, prior work has shown that DNA-bound

375 Yan monomers enhance recruitment of Yan to adjacent binding sites through stabilizing protein-
376 protein interactions (19, 40). As shown in our model, such cooperativity makes the system
377 sensitive to small but sustained relative changes, leading to non-linear (ultrasensitive and
378 threshold-like) changes in site occupancy that can drive a state transition. These general ratiometric
379 system features could be readily incorporated into transcriptional networks with more than two
380 regulators and more generally could provide robust regulation to a broad spectrum of biological
381 processes that require precise combinatorial interactions between competing regulatory factors.
382
383 An unexpected discovery in our experiments is the ability of the Pnt/Yan system to maintain a
384 fixed ratio and to make correct transitions over at least a four-fold range of activator concentration.
385 This predicts a stabilizing mechanism that monitors the relative ratio of Pnt and Yan and takes
386 corrective action when the ratio deviates from a specified reference value. The molecular nature
387 of the stabilizing mechanism in P cells and the means by which it is modified so that R cells can
388 increase and maintain an elevated ratio are currently unknown but could involve both
389 transcriptional and post-transcriptional feedback. For example, a simple way to couple Yan levels
390 to Pnt would be a positive feedback loop in which Pnt transcriptionally activates *yan*. Positive
391 feedback-based architecture is often incorporated into transcriptional regulatory circuits that
392 control cell differentiation and can filter transient fluctuations (noise) in the levels of individual
393 components to prevent random transitions (45, 46). Based on the multiple layers of positive and
394 negative feedback regulation within the Pnt/Yan network (16, 17, 30, 44, 47), more elaborate
395 mechanisms are possible.
396
397 Previous studies have found cells can sense and respond to relative concentration changes of
398 individual molecular species using fold-change detection (9, 48–53). These studies suggest that to
399 compute fold-change of a single type of protein, cells use specific regulatory circuits to first
400 "measure" and establish a molecular memory of the state of one variable, and later compare it to
401 a new measurement of the same variable (54). In contrast, cells in the eye system concurrently
402 compare the levels of two different transcription factors rather than measure the fold-change of
403 each factor over time. Identifying the specific network features that enable ratiometric detection
404 in the Pnt/Yan system and measuring the transcription response dynamics of individual target
405 genes to changes in Pnt-to-Yan ratios will provide important tests of our model. Given the broad

406 reliance of cell state transitions on combinatorial regulation, ratiometric control may prove to be a
407 common and effective developmental strategy for ensuring their accuracy and robustness.
408
409 **EXPERIMENTAL PROCEDURES**
410
411 **Genetics**
412 Unless otherwise noted, all experiments were performed with animals reared at 25ºC on standard
413 cornmeal-molasses *Drosophila* culture medium. Fly stocks from the Bloomington Stock Center:
414 *pnt-GFP* BAC transgene, BL42680; pnt^{2}, BL2222; H2Av-mRFP BL23650, $pnt^{\Delta 88}$ (21);
415 $sev>Ras^{v12}$ (37); $sev>Yan^{ACT}$ (22); *sev>Gal4* (55). Measurements of wild type dynamics of Pnt-
416 GFP were made in eye discs from w^{1118}; *pnt-GFP;* $pnt^{\Delta 88}/pnt^{2}$, *H2Av-mRFP*. The effect of *pnt* gene
417 dosage on Pnt-to-Yan ratio was measured in w^{1118}; *pnt-gfp /+ ;* $pnt^{\Delta 88}/pnt^{2}$ (1x *pnt*) and *w1118;*
418 *pnt-gfp;* $pnt^{\Delta 88}/pnt^{2}$ (2x *pnt*) discs. In experiments with Ras^{v12} or Yan^{ACT}, Pnt-GFP and Yan levels
419 were measured in eye discs from animals of the following genotypes: w^{1118}; *pnt-gfp/* $sev>Ras^{v12}$;
420 $pnt^{\Delta 88}$/+ relative to w^{1118}; *pnt-gfp / +;* $pnt^{\Delta 88}$/+; and w^{1118}; *pnt-gfp/*$sev>Yan^{ACT}$; $pnt^{\Delta 88}$/+ relative
421 to w^{1118}; *pnt-gfp/ +;* $pnt^{\Delta 88}$/+.
422
423 **Immunohistochemistry**
424
425 All eye-antennal discs were dissected from white prepupae. For experiments in which 4′,6-
426 diamidino-2-phenylindole (DAPI) was used as the nuclear marker, samples were fixed in 4%
427 paraformaldehyde (w/v) / PBS-Triton X-100 0.1% (v/v) for 25 minutes at room temperature. After
428 fixation, eye discs were blocked in PBS-Triton X-100 0.1% (v/v) and 1% (v/v) normal goat serum
429 for 30 minutes at room temperature. Primary and secondary antibodies were incubated each for 2
430 hours at room temperature with DAPI. Including DAPI during primary and secondary antibody
431 staining was important for even penetration of DAPI. Antibodies used: mouse anti-Yan 8B12
432 (DHSB, 1:200) and goat anti-mouse Cy3 (1:2000, Jackson Immunoresearch). Discs were washed
433 for 20 min in PBS-Triton X-100 0.1% (v/v), and mounted in VectaShield Antifade mounting
434 medium (Vector Laboratories). To avoid rapid changes in cell volume, which would affect relative
435 fluorescence measurements, the substitution of PBS-Triton X-100 with Vectashield was done
436 gradually using increments of ~33% in VectaShield concentration. For experiments in which

437 H2Av-mRFP was used as the nuclear marker, discs were fixed in 4% (w/v) paraformaldehyde/PBS
438 for ~45 min and goat anti-mouse Pacific Blue antibody (Life Technologies, 1:200 dilution) was
439 used as the secondary antibody.
440
441 Samples were imaged within 18-24 hr after fixation. 1024 x 1024 16-bit images were captured
442 using either a Zeiss LSM880 or a Leica SP5 confocal microscope equipped with 40X oil
443 objectives. Discs were oriented with the equator (dorsal-ventral boundary) parallel to the x-axis of
444 the image. Optical slices were set at 0.8µm (45-60 optical slices per disc) with an additional digital
445 zoom of 1.2-1.4. Images recorded a region of at least 6 rows of ommatidia on each side of the
446 equator. All discs for a given perturbation were fixed, mounted, and imaged in parallel with control
447 discs to reduce measurement error. Sample preparation, imaging, and analysis were not performed
448 under blind conditions, nor was sex of the animals noted at time of dissection.
449
450 **Quantification of expression levels**
451 A minimum of three experimental replicate eye discs were imaged for each experimental
452 condition, with the exception of the *sev>Ras*^{V12} condition for which only one control disc was
453 used. For each wild type eye disc, ~160 R8, ~320 R2/5, ~300 R3/4, ~260 R1/6, ~ 220 R7 and
454 >1000 progenitor cells were manually selected from a set of computationally 2D-segmented
455 nuclei using Silhouette. The fluorescence intensity of each nucleus was measured by our
456 established procedure (Peláez et al 2015). Our new pipeline includes Silhouette, an open-source
457 package for macOS that integrates our image segmentation algorithm with a GUI (graphical user
458 interface) for cell type annotation (available at:
459 https://www.silhouette.amaral.northwestern.edu/). Subsequent analysis and visualization
460 procedures were carried out using the accompanying FlyEye python package, which is freely
461 available on GitHub. The resulting expression dynamics were inferred from confocal image
462 stacks using an updated version of the segmentation and annotation pipeline described in (31)..
463 Empirically, the replicate number of three eye discs provided reproducible composite dynamics.
464 No outlier eye discs were found for any experimental condition, so all samples were pooled,
465 temporally aligned and included in the analysis. The sample size was not pre-computed before
466 data collection.
467

468 Nuclear segmentation was performed using either H2Av-mRFP (Figures 1, 3, 4, S1-S2, S4 and
469 S5) or DAPI (Figures 2, 5 and S7-S9) as a reference channel to identify individual nuclear
470 boundaries. Nuclei expressing H2Av-mRFP were segmented using the Silhouette app's optimized
471 implementation of the GraphCut algorithm (56), while DAPI-stained discs were segmented using
472 an open-source implementation of the watershed algorithm designed to mitigate the effect of bright
473 spots caused by DAPI accumulation in nucleoli (57). Each layer of the confocal stack was
474 segmented in 2D independently in both cases. For each nucleus measured, a single contour was
475 manually selected and assigned a cell type (cell state) using Silhouette, with care taken to avoid
476 annotating nucleolar contours rather than complete nuclear contours in DAPI-stained discs. Since
477 each nucleus spans multiple optical sections, contours were always selected in the middle of the
478 nucleus. The population of progenitor cells was measured in multiple layers to include cells whose
479 nuclei were at different positions in the Apical -Ventral axis of the eye disc. In all cases each
480 nucleus was measured only in one layer to avoid measurement pseudoreplication.
481
482 Cells were identified and annotated by nuclear position in xyz space and shape using the His2Av-
483 mRFP channel with the other channels turned off. marker protein channel turned off. To validate
484 the accuracy of this method of cell identification / annotation, cells were also immunostained for
485 various cell-type specific marker proteins, as noted in Table S1. Annotations made with tie
486 His2Av-mRFP channel were then compared to the cell-type specific markers visualized in other
487 channels.
488
489 For each annotated nucleus contour, expression measurements were obtained by normalizing the
490 mean fluorescence of the Pnt-GFP and Yan antibody channels by the mean fluorescence of the
491 reference channel used for segmentation (DAPI or His2Av-mRFP). This normalization mitigates
492 variability due to potentially uneven sample illumination, segment area, nuclear volume, and in
493 the case of His-RFP, differences in protein expression capacity between cells.
494
495 **Conversion of distance to time**
496 Cell positions along the anterior-posterior axis were mapped to developmental time as described
497 previously (31). This is predicated on two assumptions: the furrow proceeds at a constant rate of
498 one column of R8 neurons per two hours; and minimal cell migration occurs. For each disc,

499 Delaunay triangulations were used to estimate the median distance between adjacent columns of
500 R8 neurons (58). We used the median rather than the mean distance because it minimized the
501 influence of non-adjacent R8s that were falsely identified by the triangulation (31). Dividing the
502 furrow velocity of 2 h per column by this median distance yields a single conversion factor from
503 position along the anterior-posterior axis to developmental time. This factor was applied to all cell
504 measurements within the corresponding disc, yielding expression time series. Notably, these are
505 not single cell dynamics, but rather aggregate dynamics across the development time course of a
506 spatially organized cell population.
507
508 **Computation of moving averages and confidence intervals**
509 Moving averages were computed by first-order Savitzky-Golay filtration (59). This method
510 augments the simple windowing approach used in (31) by enabling visualization of expression
511 trends at early time-points that are otherwise obscured by large window sizes. A secondary first-
512 order filtration with one-fifth the original window size was applied to smooth lines for
513 visualization purposes. None of our conclusions are sensitive to our choice of filtration or
514 smoothing method. Primary window sizes of 250 and 75 cells were used for reporting the
515 expression of multipotent and differentiated cells, unless noted otherwise. Confidence intervals
516 for the moving average were inferred from the 2.5th and 97.5th percentile of ten-thousand-point
517 estimates of the mean within each window. Point estimates were generated by bootstrap
518 resampling with replacement of the expression levels within each window.
519
520 **Alignment of expression data**
521 To align multiple eye disc samples, cells of each sample were aligned with a reference
522 population by shifting them in time. The magnitude of this shift was determined by maximizing
523 the cross-correlation of progenitor Pnt-GFP expression *Y(t)* with the corresponding reference
524 time series *X(t)*. Rather than raw measurements, moving averages within a window of ten cells
525 were used to improve robustness against noise. This operation amounts to:

$$z = \underset{dt}{\operatorname{argmax}} \ \hat{\gamma}_{X(t),Y(t)}$$

$$\hat{\gamma}_{X(t),Y(t)}(dt) = E\Big[\frac{(Y(t+dt)-\mu_Y)(X(t)-\mu_X)}{\sigma_Y \sigma_X}\Big]$$

526 where, μ and σ are the mean and standard deviation of each time series, and *dt* is the time shift by
527 which the population should be shifted.

528 For each experimental treatment, a disc was randomly chosen and shifted in time such that time
529 zero corresponds to the first annotated R8 neuron. This disc then served as the reference
530 population for the alignment of all subsequent biological replicates within the treatment.
531 Similarly, different experimental treatments (e.g. control and perturbation) were aligned by first
532 aligning the discs within each treatment, then aggregating all cells within each treatment and
533 repeating the procedure with the first treatment serving as the reference.

534 This approach differs from the previous implementation of our pipeline in which discs were
535 manually aligned by the inflection point of their Yan-YFP expression profiles (31). Manual
536 alignment entails arbitrary prioritization of certain dynamic features over others. Our revised
537 protocol yields consistent, reproducible alignment of expression time series that equally weighs
538 the entire time course. The automated approach is more principled but less robust than the
539 manual approach. Specifically, it fails when dynamic forms qualitatively differ between
540 experimental treatments. In these instances, we revert to manual alignment using the inflection
541 point of Pnt-GFP induction as a reference.

542 **Simple competitive binding model**

543 Figure S10 presents results for an equilibrium model of two species, Yan (Y) and Pnt (P),
544 competing for a finite pool of shared binding sites, S:

$$Y + S \overset{K_{D,Yan}}{\Longleftrightarrow} SY$$

$$P + S \overset{K_{D,Pnt}}{\Longleftrightarrow} SP$$

545

546 where $K_{D,Yan}$ and $K_{D,Pnt}$ are equilibrium association constants and SY and SP denote the bound
547 species. Applying a mass balance to the total protein and binding site (S_0) abundances:

$$Y_0 = Y + SY$$

$$P_0 = P + SP$$

$$S_0 = S + SY + SP$$

548

549 yields an analytically tractable system of nonlinear equations (60). For each pair of absolute
550 protein abundances (Y_0, P_0), the Pnt binding site occupancy is simply SP/S_0.

551 **Competitive binding model with cooperativity**

552 The model presented in Figures 6 and S11 expands upon the work of (43). The model is based on
553 a single cis-regulatory element consisting of *n* adjacent binding sites, each of which may be
554 designated as ETS or non-ETS. Each binding site may exist in one of three binding states; bound
555 by a single copy of Yan, bound by a single copy of Pnt, or unbound. Thermodynamic potentials
556 were assigned to each binding state using two parameters for each transcription factor. The
557 parameter αX defines the free energy of transcription factor *X* binding to an ETS site,
558 while βX defines the free energy of binding to a non-ETS site. A unique configuration of binding
559 states for all *n* binding sites constitutes a single microstate, *k*. The thermodynamic potential of
560 each microstate was taken to be the sum of thermodynamic potentials for each of its constituent
561 binding sites. For each microstate, the stabilizing effect of polymerization was incorporated via a
562 third parameter, γX, that defines the free energy of SAM-SAM binding between a pair of similar
563 transcription factors bound to adjacent sites. The net result is a total thermodynamic
564 potential, ΔGk, for each microstate. An example enumeration of all possible microstates for an
565 element consisting of one ETS site preceding two non-ETS sites is provided in Figure S11B. The
566 statistical frequencies of each microstate were evaluated by constructing a canonical ensemble:

$$p_k = \frac{exp(\frac{-\Delta G_k}{RT})[P]^{a_P(k)}[Y]^{a_Y(k)}}{\sum_k exp(\frac{-\Delta G_k}{RT})[P]^{a_P(k)}[Y]^{a_Y(k)}}$$

567 in which *pk* is the statistical frequency of microstate *k, [P]* is the Pnt concentration, *[Y]* is the
568 Yan concentration, *aP(k)* and *aY(k)* are functions representing the number of bound molecules
569 of *P* and *Y* within microstate k, *T* is a fixed temperature set to 300 K, and *R* is the gas constant.
570 Fractional occupancies for each binding site correspond to the cumulative statistical frequency of
571 all microstates in which the site is occupied by a given transcription factor. Overall fractional
572 occupancies are similarly evaluated across all sites within the element.
573
574 We considered regulatory elements comprised of 12 binding sites in which only the first site
575 carries the ETS designation. We retained the same parameterization of Yan binding used by

576 (43): αY=-9.955 kcal mol^{-1}, βY=-5.837 kcal mol^{-1}, and γY=-7.043 kcal mol^{-1}. We parameterized
577 Pnt binding thermodynamics to provide balanced competition between Pnt and Yan in the
578 absence of any SAM-mediated polymerization of Pnt. That is, we set Pnt binding affinities such
579 that the transition from Pnt to Yan occupancy occurs when Pnt and Yan concentrations are
580 approximately equal. The model used to generate Figure 6B assumes that Pnt binds individual
581 sites with elevated affinities $\alpha P = 0.96(\alpha Y + \gamma Y)$ and $\beta P = 0.96(\beta Y + \gamma Y)$. The model used to
582 generate Figure 6A uses these same elevated binding affinities for Yan, while setting γY=0 kcal
583 mol^{-1}. Qualitatively, our results are not sensitive to this parameterization.
584
585 Statistical frequencies of all microstates were enumerated using a recursive graph-traversal
586 algorithm implemented in python, where each node in the graph represents an individual binding
587 site and each edge reflects occupancy by a specific transcription factor. An open-source python
588 implementation of this modeling framework has been published on GitHub
589 (https://doi.org/10.5281/zenodo.5520493).

590 **Data and software availability**

591 All segmented and annotated eye discs will be deposited in a data repository upon publication. A
592 series of Jupyter notebooks that use these data to reproduce all analysis, simulations, and figures
593 presented in this manuscript has also been made available
594 (https://github.com/sbernasek/pnt_yan_ratio).
595
596 The Silhouette app used to segment nuclei in eye discs expressing His-2Av-mRFP and annotate
597 nuclei in all eye discs is freely available via the macOS App Store, while the FlyEye python
598 package used to generate, align, and visualize expression dynamics has been published on
599 GitHub (https://doi.org/10.5281/zenodo.5520468). Data are deposited at
600 https://datadryad.org/stash/share/ FrDw4tWe_ddlP7ATp3oYEvLG6FMe_3XAvNkbp9Ma2fk.
601

602 **ACKNOWLEDGEMENTS**

603 We thank members of the Amaral, Carthew and Rebay labs for helpful discussions during the
604 course of this project. We thank Kevin White's lab and the MODEncode Consortium for

605 recombineering the Pnt-GFP transgene, the Howard Hughes Medical Institute (HHMI) and the
606 Hanna H Gray Fellowship program (N.P.), the Chicago Biomedical Consortium (N.P), the Robert
607 Lurie Northwestern Cancer Center (N.P.), the NIH (EY025957, I.R. and R.W.C; GM118144,
608 R.W.C.; GM080372, I.R.), the NSF (1764421, L.A.N.A., N.B. and R.W.C), and Simons
609 Foundation (597491 L.A.N.A., N.B. and R.W.C) for funding, the Bloomington Drosophila Stock
610 Center for flies, Laura Nilson for the use of computational resources, the Developmental Studies
611 Hybridoma Bank for antibody reagents, and the Northwestern Biological Imaging Facility (BIF)
612 for technical imaging support.

613
614 **REFERENCES**
615

616 1. U. Alon, *An introduction to systems biology: design principles of biological circuits* (CRC
617 press, 2006).

618 2. Y. Lin, C. H. Sohn, C. K. Dalal, L. Cai, M. B. Elowitz, Combinatorial gene regulation by
619 modulation of relative pulse timing. *Nature* 527, 54–58 (2015).

620 3. J. E. Purvis, G. Lahav, Encoding and Decoding Cellular Information through Signaling
621 Dynamics. *Cell* 152, 945–956 (2013).

622 4. M. A. Gillespie, *et al.*, Absolute Quantification of Transcription Factors Reveals Principles of
623 Gene Regulation in Erythropoiesis. *Mol Cell* 78, 960-974.e11 (2020).

624 5. J. L. Kopp, B. D. Ormsbee, M. Desler, A. Rizzino, Small Increases in the Level of Sox2
625 Trigger the Differentiation of Mouse Embryonic Stem Cells. *Stem Cells* 26, 903–911 (2008).

626 6. P. Laslo, *et al.*, Multilineage Transcriptional Priming and Determination of Alternate
627 Hematopoietic Cell Fates. *Cell* 126, 755–766 (2006).

628 7. H. Niwa, J. Miyazaki, A. G. Smith, Quantitative expression of Oct-3/4 defines differentiation,
629 dedifferentiation or self-renewal of ES cells. *Nat Genet* 24, 372–376 (2000).

630 8. C. L. Frick, C. Yarka, H. Nunns, L. Goentoro, Sensing relative signal in the Tgf-β/Smad
631 pathway. *Proc National Acad Sci* 114, E2975–E2982 (2017).

632 9. L. Goentoro, M. W. Kirschner, Evidence that Fold-Change, and Not Absolute Level, of β-
633 Catenin Dictates Wnt Signaling. *Mol Cell* 36, 872–884 (2009).

634 10. G. V. Flores, *et al.*, Combinatorial signaling in the specification of unique cell fates. *Cell*
635 103, 75–85 (2000).

636 11. M. S. Halfon, *et al.*, Ras pathway specificity is determined by the integration of multiple
637 signal-activated and tissue-restricted transcription factors. *Cell* 103, 63–74 (2000).

638 12. C. Xu, R. C. Kauffmann, J. Zhang, S. Kladny, R. W. Carthew, Overlapping activators and
639 repressors delimit transcriptional response to receptor tyrosine kinase signals in the Drosophila
640 eye. *Cell* 103, 87–97 (2000).

641 13. L. J. Zhu, *et al.*, FlyFactorSurvey: a database of Drosophila transcription factor binding
642 specificities determined using the bacterial one-hybrid system. *Nucleic Acids Res* 39, D111–
643 D117 (2011).

644 14. G. Wei, *et al.*, Genome-wide analysis of ETS-family DNA-binding in vitro and in vivo.
645 *Embo J* 29, 2147–2160 (2010).

646 15. K. R. Nitta, *et al.*, Conservation of transcription factor binding specificities across 600
647 million years of bilateria evolution. *Elife* 4, e04837 (2015).

648 16. J. L. Webber, J. Zhang, A. Massey, N. Sanchez-Luege, I. Rebay, Collaborative repressive
649 action of the antagonistic ETS transcription factors Pointed and Yan fine-tunes gene expression
650 to confer robustness in Drosophila. *Development* 145, dev165985 (2018).

651 17. J. L. Webber, *et al.*, The Relationship between Long-range Chromatin Occupancy and
652 Polymerization of the Drosophila ETS Family Transcriptional Repressor Yan. *Genetics*, 633–649
653 (2013).

654 18. J. L. Webber, J. Zhang, A. Mitchell-Dick, I. Rebay, 3D chromatin interactions organize Yan
655 chromatin occupancy and repression at the even-skipped locus. *Genes Dev* 27, 2293–2298
656 (2013).

657 19. J.-F. B. Lachance, J. L. Webber, L. Hong, A. R. Dinner, I. Rebay, Cooperative recruitment of
658 Yan via a high-affinity ETS supersite organizes repression to confer specificity and robustness to
659 cardiac cell fate specification. *Gene Dev* 32, 389–401 (2018).

660 20. P. C. Hollenhorst, L. P. McIntosh, B. J. Graves, Genomic and Biochemical Insights into the
661 Specificity of ETS Transcription Factors. *Annu Rev Biochem* 80, 437–471 (2011).

662 21. E. M. O'Neill, I. Rebay, R. Tjian, G. M. Rubin, The activities of two Ets-related transcription
663 factors required for Drosophila eye development are modulated by the Ras/MAPK pathway. *Cell*
664 78, 137–147 (1994).

665 22. I. Rebay, G. M. Rubin, Yan functions as a general inhibitor of differentiation and is
666 negatively regulated by activation of the Ras1/MAPK pathway. *Cell* 81, 857–866 (1995).

667 23. A. Shwartz, S. Yogev, E. D. Schejter, B. Z. Shilo, Sequential activation of ETS proteins
668 provides a sustained transcriptional response to EGFR signaling. *Development* 140, 2746–2754
669 (2013).

670 24. G. J. Melen, S. Levy, N. Barkai, B. Z. Shilo, Threshold responses to morphogen gradients by
671 zero-order sensitivity. *Molecular Systems Biology* 10, 1–11 (2005).

672 25. R. Rogge, *et al.*, The role ofyanin mediating the choice between cell division and
673 differentiation. *Development* 121, 3947–3958 (1995).

674 26. L. Gabay, *et al.*, EGF receptor signaling induces pointed P1 transcription and inactivates Yan
675 protein in the Drosophila embryonic ventral ectoderm. *Development* 122, 3355–62. (1996).

676 27. L. Gabay, R. Seger, B. Z. Shilo, MAP kinase in situ activation atlas
677 duringDrosophilaembryogenesis. *Development* 124, 3535–3541 (1997).

678 28. J. F. B. Lachance, *et al.*, A comparative study of Pointed and Yan expression reveals new
679 complexity to the transcriptional networks downstream of receptor tyrosine kinase signaling. *Dev*
680 *Biol* 385, 263–278 (2014).

681 29. M. Freeman, Reiterative use of the EGF receptor triggers differentiation of all cell types in
682 the Drosophila eye. *Cell* 87, 651–60. (1996).

683 30. C. Wu, J.-F. B. Lachance, M. Z. Ludwig, I. Rebay, A context-dependent bifurcation in the
684 Pointed transcriptional effector network contributes specificity and robustness to retinal cell fate
685 acquisition. *Plos Genet* 16, e1009216 (2020).

686 31. N. Peláez, *et al.*, Dynamics and heterogeneity of a fate determinant during transition towards
687 cell differentiation. *Elife* 4, e08924 (2015).

688 32. J. E. Treisman, Retinal differentiation in Drosophila. *Wiley Interdiscip Rev Dev Biol* 2, 545–
689 557 (2013).

690 33. M. G. Voas, I. Rebay, Signal integration during development: insights from the Drosophila
691 eye. *Dev Dyn* 229, 162–175 (2004).

692 34. A. Tomlinson, D. F. Ready, Cell Fate in the Drosophila Ommatidium. *Developmental*
693 *biology* 123, 264–275 (1987).

694 35. T. Wolff, D. F. Ready, Pattern Formation in the Drosophila Retina. *Cold Spring Harbor*
695 *Laboratory Press*, 1277–1325 (1993).

696 36. K. D. Gallagher, M. Mani, R. W. Carthew, Emergence of a geometric pattern of cell fates
697 from tissue-scale mechanics in the Drosophila eye. *Elife* 11, e72806 (2022).

698 37. M. E. Fortini, M. A. Simon, G. M. Rubin, Signalling by the sevenless protein tyrosine kinase
699 is mimicked by Ras1 activation. *Nature* 355, 559–561 (1992).

700 38. M. A. Simon, D. D. Bowtell, G. S. Dodson, T. R. Laverty, G. M. Rubin, Ras1 and a putative
701 guanine nucleotide exchange factor perform crucial steps in signaling by the sevenless protein
702 tyrosine kinase. *Cell* 67, 701–716 (1991).

703 39. T. L. Tootle, P. S. Lee, I. Rebay, CRM1-mediated nuclear export and regulated activity of
704 the Receptor Tyrosine Kinase antagonist YAN require specific interactions with MAE.
705 *Development* 130, 845–857 (2003).

706 40. F. Qiao, *et al.*, Derepression by depolymerization: Structural insights into the regulation of
707 Yan by Mae. *Cell* 118, 163–173 (2004).

708 41. C. D. Mackereth, *et al.*, Diversity in structure and function of the Ets family PNT domains. *J*
709 *Mol Biol* 342, 1249–1264 (2004).

710 42. A. D. Meruelo, J. U. Bowie, Identifying polymer-forming SAM domains. *Proteins* 74, 1–5
711 (2009).

712 43. C. M. Hope, I. Rebay, J. Reinitz, DNA Occupancy of Polymerizing Transcription Factors: A
713 Chemical Model of the ETS Family Factor Yan. *Biophys J* 112, 180–192 (2017).

714 44. T. G. W. Graham, S. M. A. Tabei, A. R. Dinner, I. Rebay, Modeling bistable cell-fate
715 choices in the Drosophila eye: qualitative and quantitative perspectives. *Development* 137, 2265–
716 2278 (2010).

717 45. G. Balázsi, A. van Oudenaarden, J. J. Collins, Cellular Decision Making and Biological
718 Noise: From Microbes to Mammals. *Cell* 144, 910–925 (2011).

719 46. G. Chalancon, *et al.*, Interplay between gene expression noise and regulatory network
720 architecture. *Trends Genet* 28, 221–232 (2012).

721 47. M. Rohrbaugh, *et al.*, Notch Activation of yan Expression Is Antagonized by RTK/Pointed
722 Signaling in the Drosophila Eye. *Curr Biol* 12, 576–81. (2002).

723 48. R. Mesibov, G. W. Ordal, J. Adler, The Range of Attractant Concentrations for Bacterial
724 Chemotaxis and the Threshold and Size of Response over This Range. *J Gen Physiology* 62,
725 203–223 (1973).

726 49. N. Barkai, S. Leibler, Robustness in simple biochemical networks. *Nature* 387, 913–917
727 (1997).

728 50. R. E. Lee, S. R. Walker, K. Savery, D. A. Frank, S. Gaudet, Fold change of nuclear NF-
729 kappaB determines TNF-induced transcription in single cells. *Mol Cell* 53, 867–879 (2014).

730 51. C. Cohen-Saidon, A. A. Cohen, A. Sigal, Y. Liron, U. Alon, Dynamics and Variability of
731 ERK2 Response to EGF in Individual Living Cells. *Mol Cell* 36, 885–893 (2009).

732 52. O. Shoval, *et al.*, Fold-change detection and scalar symmetry of sensory input fields. *Proc*
733 *National Acad Sci* 107, 15995–16000 (2010).

734 53. U. Alon, M. G. Surette, N. Barkai, S. Leibler, Robustness in bacterial chemotaxis. *Nature*
735 397, 168–171 (1999).

736 54. E. Lyashenko, *et al.*, Receptor-based mechanism of relative sensing and cell memory in
737 mammalian signaling networks. *Elife* 9, e50342 (2020).

738 55. J. Jemc, I. Rebay, Characterization of the split ends-like gene spenito reveals functional
739 antagonism between SPOC family members during Drosophila eye development. *Genetics* 173,
740 279–286 (2006).

741 56. J. QI, Dense nuclei segmentation based on graph cut and convexity-concavity analysis:
742 DENSE NUCLEI SEGMENTATION. *J Microsc-oxford* 253, 42–53 (2013).

743 57. S. M. Bernasek, N. Peláez, R. W. Carthew, N. Bagheri, L. A. N. Amaral, Fly-QMA:
744 Automated analysis of mosaic imaginal discs in Drosophila. *Plos Comput Biol* 16, e1007406
745 (2020).

746 58. Fortune, Steven, Voronoi Diagrams and Delaunay Triangulations. *Computing in Euclidean*
747 *Geometry* (1992) https:/doi.org/Fortune, Steven.

748 59. Abraham. Savitzky, M. J. E. Golay, Smoothing and Differentiation of Data by Simplified
749 Least Squares Procedures. *Analytical Chemistry* (1964)
750 https:/doi.org/doi.org/10.1021/ac60214a047.

751 60. Z.-X. Wang, An exact mathematical expression for describing competitive binding of two
752 different ligands to a protein molecule. *Febs Lett* 360, 111–114 (1995).

753
754
755
756 **FIGURE LEGENDS**
757
758 **Figure 1. Measuring Pnt and Yan expression in thousands of single cells defines two waves**
759 **of cell state transitions**
760
761 **(A)** Schematic summary of RTK-mediated regulation of P to R fate transitions. Poised P cells co-
762 express Pnt and Yan in their nuclei (left panel). In response to a strong RTK signal, young R cells
763 increase Pnt and decrease Yan (right panel).
764 **(B)** Schematic of a developing eye imaginal disc dissected from an animal ∼100 hours post
765 fertilization (25°C). Differentiation is initiated by passage of the morphogenetic furrow (MF),
766 which moves across the eye epithelium from posterior to anterior (white arrow). Anterior P cells
767 (dark blue) proliferate asynchronously, while P cells posterior to the furrow (light blue) arrest in
768 G1, and some of them undergo a stereotyped sequence of state transitions. Specification of

769 regularly spaced R8 cells (red dots) marks the start of ommatidial assembly and is followed by
770 recruitment of additional R cell types (yellow dots). Adapted from Peláez et al. (2015).
771 **(C)** Maximum intensity projection of Pnt-GFP fluorescence in wild type eye disc oriented anterior
772 to the left and dorsal up. Right panel shows zoomed view of region marked by dashed white lines.
773 Arrival of the MF (white arrow) initiates cell fate transitions in the regions marked by the two
774 pulses of peak Pnt-GFP expression (black bars, labeled 1 and 2). Anterior-ward movement of the
775 MF allows tracking of P to R1-R8 cell state transitions across developmental time.
776 **(D-E)** Measured **(D)** Pnt-GFP and **(E)** Yan expression dynamics in individual P cell (grey) and R7
777 cell (purple) nuclei. P cells are present across the entire developmental time (grey arrow). A subset
778 transition to R7 cells which persist over time (purple arrow). Solid black lines are smoothed
779 moving averages across 250 and 75 individual nuclei for P and R7 cells, respectively. Black bars
780 labeled 1 and 2 denote the two pulses of peak Pnt-GFP in P cells. Shaded vertical stripes highlight
781 these two regions, which coincide with transition of P to various R fates shown in **F- I**.
782 **(F-I)** Dynamics of **(F,H)** Pnt-GFP and **(G,I)** Yan expression in **(F,G)** R8 (green), R2/R5 (blue)
783 and R3/R4 (orange) cells and **(H,I)** R1/R6 (red) and R7 (purple) cells. Grey denotes P cells. Lines
784 are smoothed moving averages across individual nuclei, backed by 95% confidence intervals for
785 the mean. Subsets of P cells transition into distinct R fates at different time points and span the
786 developmental time from thereafter, as indicated by colored arrows.
787
788 **Figure 2. Pnt-to-Yan ratio in P cells buffers against reduced Pnt dosage**
789
790 **(A-D)** Moving averages of **(A, C)** Pnt-GFP and **(B, D)** Yan expression levels in P and R cells with
791 two copies **(A, B)** versus one copy **(C, D)** of the *pnt-GFP* gene. Measurements were made from
792 segmented nuclei marked by DAPI. Colors denote cell type. Shaded regions are bootstrapped 95%
793 confidence intervals for the moving averages (solid lines).
794 **(E)** Comparison of Pnt-to-Yan ratios between P cells with one copy (1x, light grey filled boxes)
795 versus two copies (2x, dark grey filled boxes) of *pnt-GFP* during time-windows of cell fate
796 transitions. Colors denote transition periods for each R cell type. These time periods were defined
797 in each disc by the times spanned by the first ten identifiable R cells. The concurrent P cell
798 populations were measured from these time windows. Pnt-to-Yan ratios in P cells are statistically
799 indistinguishable between gene dosages during R8, R2/R5, and R1/R6 cell fate transitions ($P>0.1$,
800 KS 2-sample test).
801

802 **Figure 3. Increased Pnt-to-Yan ratio accompanies P to R fate transitions**
803
804 **(A)** Log2-transformed Pnt-to-Yan ratio dynamics in P (grey) and R7 (purple) cells with their
805 moving averages (solid black lines). Young R7 cells are the earliest subset of R7 cells that are
806 present in the timespan of the first ten identifiable R7 cells.
807 **(B-F)** Joint distributions of Pnt-GFP and Yan protein levels for young **(B)** R7, **(C)** R8, **(D)** R2/R5,
808 **(E)** R3/R4, and **(F)** R1/R6 cells. For each R cell type, the ten earliest identifiable R cells in each
809 sample mark the time span of young R cells. Progenitor cells that fall within the time window
810 spanned by these young R cells were designated as concurrent progenitors (grey). Black line
811 denotes the median Pnt-to-Yan ratio among the progenitor cells shown.
812 **(G)** Comparison of Pnt-to-Yan ratio levels between young R cells (color filled boxes) and their
813 concurrent progenitors (grey filled boxes). Colors denote R cell types. Asterisks indicate
814 significant differences ($P<0.001$, KS 2-sample test).

815
816 **Figure 4. Ectopic increase in Pnt-to-Yan ratio biases P cells towards R fates**
817 **(A)** Schematic of the sev>Ras^{V12} perturbation in a subset of P cells, as well as R7 and R3/R4
818 cells. **(B-D)** The effects of Ras^{V12} signaling on **(B)** Pnt-GFP and **(D)** Yan in P cells increases the
819 **(C)** Pnt-to-Yan ratio. Lines are moving averages across 250 sequential cells. Shaded regions are
820 bootstrapped 95% confidence intervals for the mean. Solid lines and grey shading denote wildtype
821 controls. Dashed lines and red shading denote constitutive Ras signaling by *sev>Ras^{V12}*. Black
822 bars denote the second Pnt-GFP pulse which overlaps with the period of P to R7 fate transitions.
823 Red lines indicate the time period spanned by Ras^{V12} expressing cells. We previously reported a
824 modest increase in the duration of Yan-YFP expression in *sev>Ras^{V12}* P cells (Peláez et al. 2015),
825 but this difference was not detected using the Yan antibody. **(E)** Comparison of Pnt-to-Yan ratios
826 between wildtype and *sev>Ras^{V12}* P cells (grey filled box) concurrent with young R7 cells (purple
827 bordered box) as well as the first 24 ectopic unidentified R cells (light blue bordered box) in
828 *sev>Ras^{V12}* discs.
829

830 **Figure 5. Failure to increase the Pnt-to-Yan ratio biases P cells against R fates**
831 **(A)** Schematic of *sev>Yan^{ACT}* that expresses MAPK-resistant Yan^{Act} protein in a subset of P cells,
832 as well as R7 and R3/R4 cells. **(B-C)** Dynamics of the log-2 transformed Pnt-to-Yan ratio in P
833 and R7 cells in **(B)** wildtype control and **(C)** *sev>yan^{ACT}* discs. Solid black lines are moving
834 averages across 250 and 75 sequential cells for P cells (grey dots) and R7 cells (purple dots),
835 respectively. Black bars denote the second Pnt-GFP pulse which overlaps with the period of P to
836 R7 fate transitions. Red lines indicate the time period spanned by Yan^{Act} expressing cells.
837 **(D)** Comparison of the Pnt-to-Yan ratios in P cells concurrent with remaining R7 cells in
838 *sev>Yan^{ACT}* discs. We include all P and R7 cells observed between 15 and 20 h
839 in **(B,C)**. **(E)** Cumulative abundance of each annotated R cell type as a function of developmental
840 time in wildtype (top) and *sev>Yan^{ACT}* (bottom) discs. Counts are normalized by the total number
841 of R8 cells detected across the time-course, and R2, R5, R3, R4, R1, and R6 cells are each tallied
842 separately. Colors denote R cell type. Shading denotes bootstrapped 95% confidence intervals for
843 each contour. R7 cells were not detected in approximately 85% of *sev>Yan^{ACT}* ommatidia.
844
845

846 **Figure 6. Cooperative DNA-binding by Yan sensitizes enhancer occupancy to the Pnt-to-Yan**
847 **ratio**
848 **(A)** Illustration of the competition between Pnt and Yan for occupancy of mutual binding sites in
849 the absence of Yan polymerization (left). Overall binding site occupancy calculated as a function
850 of transcription factor abundance in the absence of Yan polymerization (right).
851 Color scale reflects overall Pnt site occupancy. We use a diverging scale because all sites are
852 fully saturated at total transcription factor concentrations above 1 nM. Under the range of
853 conditions shown, this implies that Yan occupies all sites left vacant by Pnt. Simultaneous
854 proportional increases in absolute abundance of both species have minimal impact on Pnt
855 occupancy (dashed arrow), while varying ratio confers gradual change (solid arrow).
856 **(B)** Illustration of competition between Pnt and Yan for occupancy of mutual binding sites when
857 Yan polymerizes (left). Overall binding site occupancy calculated as a function of transcription
858 factor abundance when Yan polymerizes (right). Color scale and arrows as in **(A)**. Note how the
859 sharpness of the transition is greatly increased when Yan polymerizes.

860 **(C)** Average Pnt occupancy across all binding sites as a function of Pnt-to-Yan ratio in the
861 absence of Yan polymerization (black line) vs. when Yan polymerizes (pink line). The contours
862 correspond to vertical paths traversed across panel **A** (right) and panel **B** (right) at a fixed Yan
863 concentration of 50 nM. Also see Figure S11.
864 **(D)** Probability density function of measured Pnt-GFP and Yan levels for the combined
865 populations of all young R cells (red) and their concurrent P cells (black). Contours decrease in
866 opacity with decreasing density and are not shown for values below 0.1. Density function is
867 estimated using Gaussian kernels with a bandwidth selected using Scott's rule. Thin diagonal
868 line of constant Pnt-GFP-to-Yan ratio is shown to aid interpretation
869 **(E)** Mean measured Pnt-GFP and Yan levels for the combined populations of all young R cells
870 (red) and their concurrent P cells (black), sampled from eye discs containing either one (*1x Pnt*)
871 or two (*2x Pnt*) gene copies of *pnt-GFP*. Horizontal and vertical lines about each point denote
872 the standard errors of the means.
873
874 **SUPPLEMENTARY FIGURE LEGENDS**
875
876 **Figure S1. Identification of cell nuclei in eye discs.**
877 **(A)** Top, cartoon of an apical view of the sequential differentiation of the eight R cell types (R1-
878 R8, various colors) from multipotent P cells (grey) and their relative positions within a single
879 ommatidium. Arrows denote RTK signals transmitted from the R8 to nearby P cells. Bottom, a
880 cross-section view through an eye disc, showing the epithelial constriction that marks the MF
881 (boxed region) and then the relative apical-basal nuclear positions of P cells (grey) and specified
882 R cells (various colors). Together, these and other stereotyped features enable unambiguous
883 identification of each cell type. Adapted from Peláez et al. (2015).
884 **(B-F)** Quantitative analysis pipeline showing microscopy and segmentation of a representative
885 eye disc. **(B)** Partial cross-section of a confocal z-stack, with separate fluorescence channels
886 for **(C)** Histone-RFP, **(D)** Pnt-GFP, and **(E)** Yan antibody. Yellow lines depict nuclear contours
887 identified by FlyEye Silhouette. **(F)** Manual annotation of R cell types. Image shows a maximum
888 intensity projection of His-RFP fluorescence across four layers spanning early R cells. R cell
889 types are readily distinguished by their morphological positions within each ommatidium.
890
891 **Figure S2. Pnt-GFP and Yan expression in P cells.**
892 **(A)** Simultaneous Pnt-GFP (green) and Yan (magenta) expression dynamics in P cells. Lines are
893 smoothed moving averages across 500 sequential progenitors, shaded regions are bootstrapped
894 95% confidence intervals for the mean. Arrows indicate the times at which local maxima occur.
895 Note the peaks of Pnt and Yan take place sequentially in P cells.
896 **(B, C)** Expression levels of **(B)** Pnt-GFP and **(C)** Yan in P cells, color-coded in accordance with
897 the expression level of the complementary transcription factor. In both panels, markers are
898 arranged such that nuclei with higher levels of the complementary transcription factor are
899 displayed in front. Lines are smoothed moving averages across 500 sequential P cells.
900
901 **Figure S3. Characterization of Pnt-GFP**
902 Adult eyes of flies carrying **(A)** one or **(B)** two copies of the *pnt-gfp* transgene in a *pnt* null
903 mutant background have wildtype retinal patterning.
904
905 **Figure S4. Pnt expression, Yan expression and Pnt-to-Yan ratio dynamics**

(A) Measured Pnt-to-Yan ratio dynamics for all annotated cell types. Solid lines are moving averages across 250 and 75 sequential cells for P and R cells, respectively. Shading denotes bootstrapped 95% confidence interval for the moving average. Colors denote cell type. **(B-D)** Pnt and Yan expression dynamics and Pnt-to-Yan ratio dynamics for differentiating **(B^1-B^3)** R8, **(C^1-C^3)** R2/R5, **(D^1-D^3)** R3/R4, and **(E^1-E^3)** R1/R6 cells. Solid lines are smoothed moving averages across 250 and 50 samples for P and R cells, respectively.

Figure S5. Dynamics of expression variability in P, R8, R2/R5, and R1/R6 cells.
Heterogeneities of **(A)** Pnt expression, **(B)** Yan expression, and **(C)** the log2-transformed Pnt-to-Yan ratio are estimated by de-trending fluctuations about a moving average of 250 sequential cells. Lines are moving averages of 250 sequential fluctuations. Shaded regions are bootstrapped 95% confidence intervals for the moving average. Colors denote cell type.

Figure S6. sev>Gal4 drives expression in subsets of P cells.
Projection of *sev-Gal4>UAS-NLS-mCherry* protein expression (red) and DAPI (blue) in apical z-slices containing R cell nuclei and basal z-slices containing progenitor cell nuclei. Anterior left and MF is morphogenetic furrow. **(A)** Expression from a weak *sev-Gal4* driver. **(B)** Expression from a strong *sev-Gal4* driver. Scale bar denotes 20 µm. When expressed from the weak driver, mCherry is predominantly limited to R7, R3, and R4 cells. When expressed from the strong driver, mCherry is also detected in some P cells.

Figure S7. R7 phenotype in *sev>Ras^{V12}* and *sev>Yan^{ACT}*.
Antibody staining of Prospero in 9-10 ommatidia in the equivalent posterior region of the eye disc from **(A)** wildtype, **(B)** *sev>Ras^{V12}*, and **(C)** *sev>Yan^{ACT}* animals. R7 cell is marked based on stereotypical nuclear position. Extra R cells on each side of the R7 are marked as "R" in the *sev>Ras^{V12}* disc.

Figure S8. Yan^{ACT} has little to no effect on Pnt-to-Yan ratio dynamics in R8, R2/R5 or R1/R6 cells but has a moderate effect on R3/R4 cells.
(A-H) Measured Pnt-to-Yan ratio dynamics among differentiating R cells in wildtype (top row) and weak *sev>yan^{ACT}* (bottom row) eye discs. Solid black and yellow lines are moving averages across 250 and 75 sequential cells for P and R7 cells, respectively. Colors denote R cell type.

Figure S9. Yan^{ACT} has no effect on the Pnt-to-Yan ratio in P cells but does affect the ratio in R7 cells.
(A-C) Effects of weak *sev>Yan^{ACT}* expression on **(A)** Pnt-GFP, **(B)** Yan, and **(C)** the Pnt-to-Yan ratio in P cells. Lines are moving averages across 250 sequential cells. Shaded regions are bootstrapped 95% confidence intervals for the mean. Solid lines and grey shading denote wildtype controls. Dashed lines and red shading denote *sev>Yan^{ACT}*. **(D)** Joint distribution of measured Pnt and Yan levels among R7 cells sampled from the region spanning 15 to 20 h of developmental time. The *sev>yan^{ACT}* R7 cells showed higher Yan levels ($P<.001$, KS 2-sample test), while Pnt levels were indistinguishable from wildtype ($P=.4$, KS 2-sample test).

Figure S10. A simple model of Yan / Pnt competition for DNA binding sites.
Schematic of a simple two-species competitive binding model (left), alongside theoretical Pnt site occupancy as a function of transcription factor abundance (right). Equivalent binding

952 affinities are used for illustrative purposes. Color scale reflects overall Pnt site occupancy. A
953 diverging scale was used because all sites are fully saturated at total transcription factor
954 concentrations above 1 nM. Under the range of conditions shown, this implies that Yan occupies
955 all sites left vacant by Pnt. Simultaneous proportional increases in absolute abundance of both
956 species have minimal impact on Pnt occupancy (dashed arrow), while varying ratio confers
957 gradual change in occupancy (solid arrow).
958
959 **Figure S11. Cooperative DNA-binding sensitizes transcriptional output to the Pnt-to-Yan**
960 **ratio.**
961 **(A)** Summary of thermodynamic interactions within one microstate of a cis-regulatory element
962 containing one ETS site and two non-ETS sites. Solid black lines represent individual binding
963 sites. Green and magenta rectangles denote Pnt and Yan molecules. Example thermodynamic
964 potentials of strong ETS-binding, weak non-ETS binding, and polymerization interactions are
965 denoted by αPnt, βYan, and γYan, respectively. For this microstate, $aP(k)$=1 and $aY(k)$=2.
966 **(B)** Enumeration of all possible microstates for a cis-regulatory element of length 3 in which
967 only the first site carries the ETS designation. Solid black lines denote binding sites, green and
968 magenta rectangles denote bound Pnt and Yan molecules. The cumulative thermodynamic
969 potentials of each microstate, ΔGk, are listed beside each graphical depiction.
970 **(C)** Pnt occupancy of individual binding sites as a function of Pnt-to-Yan ratio in the absence of
971 Yan polymerization. Contours correspond to a vertical path traversed across Figure 6A at a fixed
972 Yan concentration of 50 nM. All binding sites behave similarly.
973 **(D)** Relative thermodynamic contributions of binding site affinity versus polymerization to
974 microstate statistical frequencies as a function of Pnt and Yan concentration. For each point in
975 the plane, the influence of site affinity was calculated by weighting the sum of all ETS and non-
976 ETS thermodynamic potentials for each microstate by the statistical frequency of the
977 corresponding microstate. The influence of polymerization was similarly determined. The color
978 scale reflects the relative magnitude of these two summations, normalized by limits of zero and
979 complete polymerization.
980 **(E)** Pnt occupancy of individual binding sites as a function of Pnt-to-Yan ratio when Yan
981 polymerizes. Contours correspond to a vertical path traversed across Figure 6B at a fixed Yan
982 concentration of 50 nM. Line colors reflect binding site positions within the cis-regulatory
983 element. Sites at intermediate distances from the strong ETS site (green lines) transition at higher
984 ratios than those nearest and furthest from the strong ETS site (blue and yellow lines).
985

Figure 1

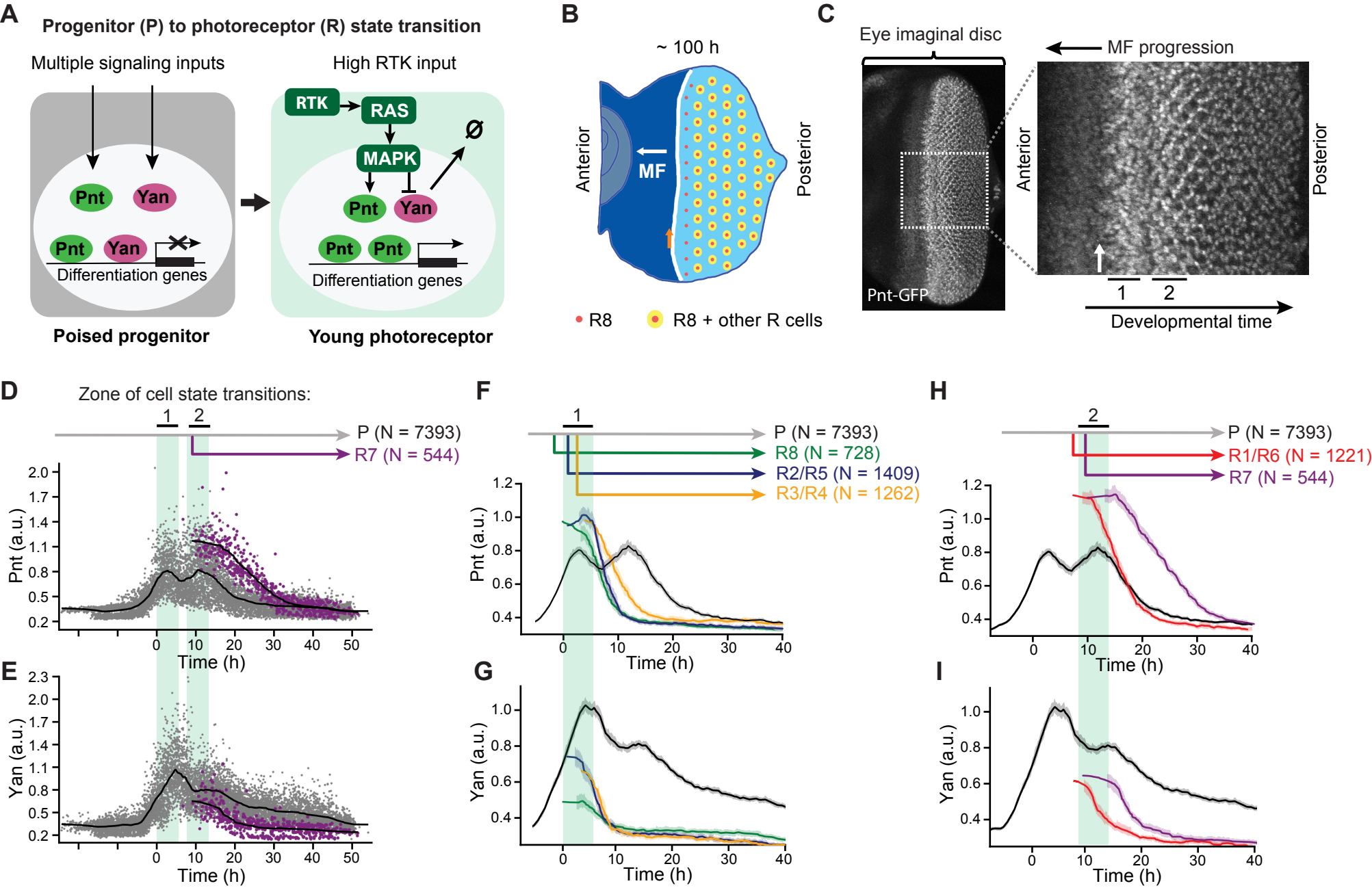
A
Progenitor (P) to photoreceptor (R) state transition
Multiple signaling inputs
High RTK input
Pnt
Yan
Pnt
Yan
Differentiation genes
RTK
RAS
MAPK
Ø
Pnt
Yan
Pnt
Pnt
Differentiation genes
Poised progenitor
Young photoreceptor
B
~ 100 h
Anterior
MF
Posterior
R8
R8 + other R cells
C
Eye imaginal disc
MF progression
Anterior
Posterior
Pnt-GFP
1
2
Developmental time
D
Zone of cell state transitions:
1
2
P (N = 7393)
R7 (N = 544)
Pnt (a.u.)
Time (h)
E
Yan (a.u.)
Time (h)
F
1
P (N = 7393)
R8 (N = 728)
R2/R5 (N = 1409)
R3/R4 (N = 1262)
Pnt (a.u.)
Time (h)
G
Yan (a.u.)
Time (h)
H
2
P (N = 7393)
R1/R6 (N = 1221)
R7 (N = 544)
Pnt (a.u.)
Time (h)
I
Yan (a.u.)
Time (h)

Figure 2

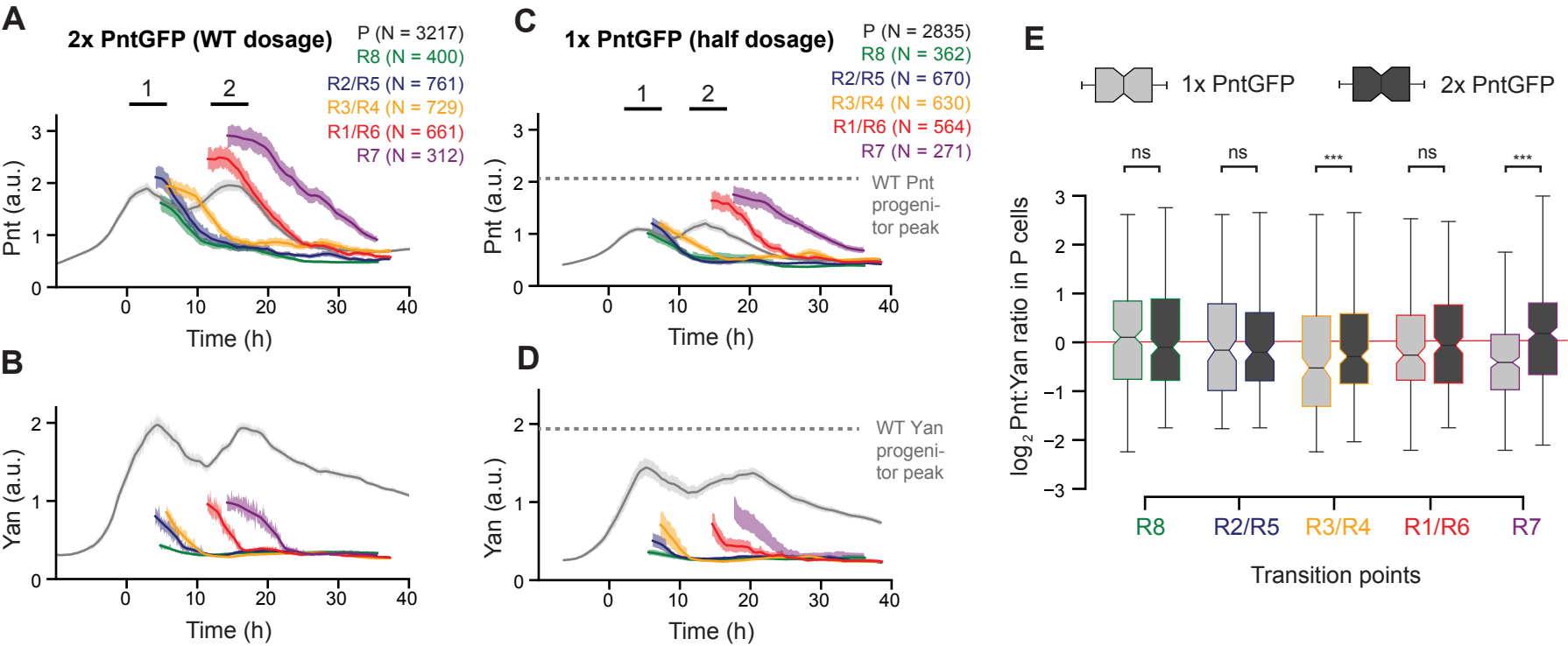
A
2x PntGFP (WT dosage)
P (N = 3217)
R8 (N = 400)
R2/R5 (N = 761)
R3/R4 (N = 729)
R1/R6 (N = 661)
R7 (N = 312)
1
2
Pnt (a.u.)
Time (h)
B
Yan (a.u.)
Time (h)
C
1x PntGFP (half dosage)
P (N = 2835)
R8 (N = 362)
R2/R5 (N = 670)
R3/R4 (N = 630)
R1/R6 (N = 564)
R7 (N = 271)
WT Pnt progenitor peak
D
WT Yan progenitor peak
E
1x PntGFP
2x PntGFP
ns
ns
***
ns
***
log2 Pnt:Yan ratio in P cells
R8
R2/R5
R3/R4
R1/R6
R7
Transition points

Figure 3

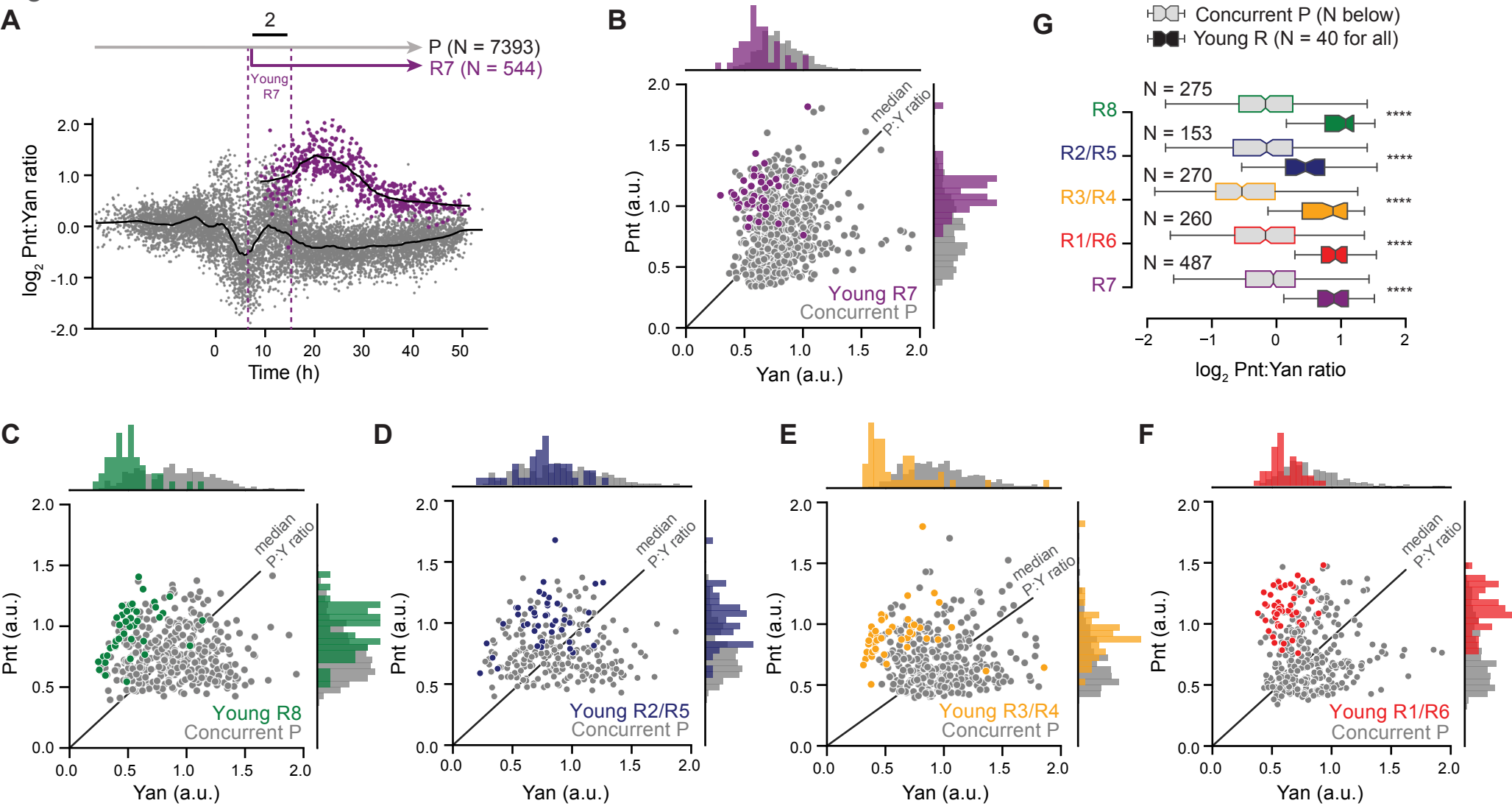
A
2
P (N = 7393)
R7 (N = 544)
Young R7
log2 Pnt:Yan ratio
Time (h)
B
median P:Y ratio
Pnt (a.u.)
Yan (a.u.)
Young R7
Concurrent P
G
Concurrent P (N below)
Young R (N = 40 for all)
R8
R2/R5
R3/R4
R1/R6
R7
N = 275
N = 153
N = 270
N = 260
N = 487
****
log2 Pnt:Yan ratio
C
Young R8
Concurrent P
D
Young R2/R5
Concurrent P
E
Young R3/R4
Concurrent P
F
Young R1/R6
Concurrent P

Figure 4

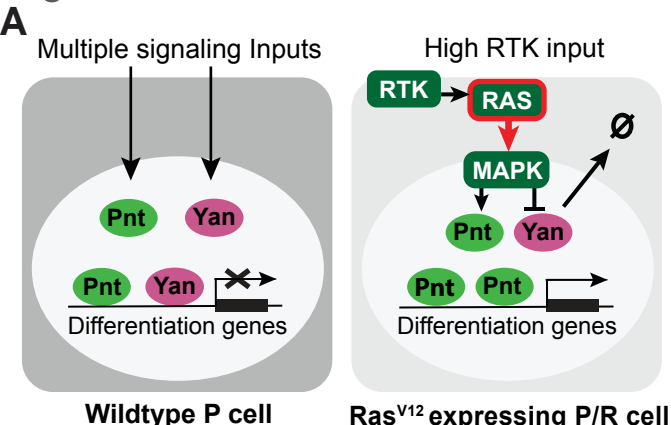
A
Multiple signaling Inputs
High RTK input
RTK
RAS
MAPK
Ø
Pnt
Yan
Pnt
Yan
Differentiation genes
Pnt
Yan
Pnt
Pnt
Differentiation genes
Wildtype P cell
Ras^{V12} expressing P/R cell

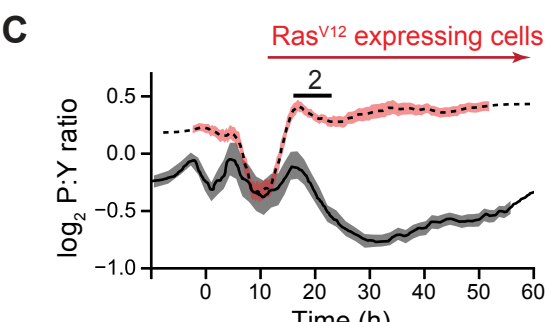
C
Ras^{V12} expressing cells
2
log$_2$ P:Y ratio
0.5
0.0
−0.5
−1.0
0
10
20
30
40
50
60
Time (h)

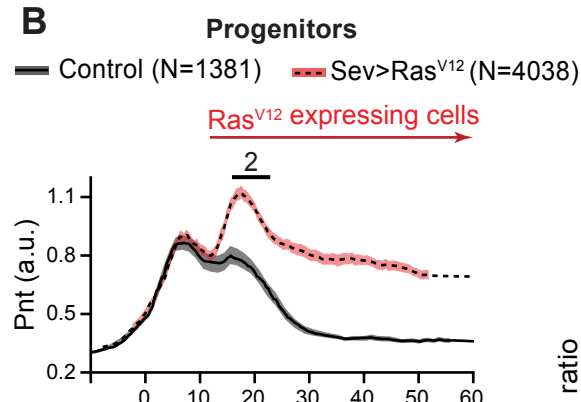
B
Progenitors
Control (N=1381)
Sev>Ras^{V12} (N=4038)
Ras^{V12} expressing cells
2
Pnt (a.u.)
1.1
0.8
0.5
0.2
0
10
20
30
40
50
60

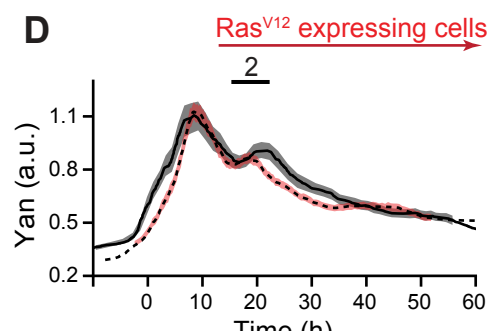
D
Ras^{V12} expressing cells
2
Yan (a.u.)
1.1
0.8
0.5
0.2
0
10
20
30
40
50
60
Time (h)

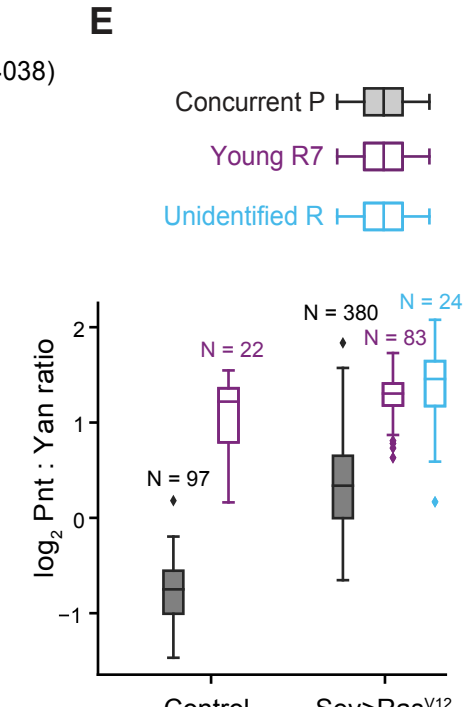
E
Concurrent P
Young R7
Unidentified R
log$_2$ Pnt : Yan ratio
2
1
0
−1
N = 97
N = 22
N = 380
N = 83
N = 24
Control
Sev>Ras^{V12}

Figure 5

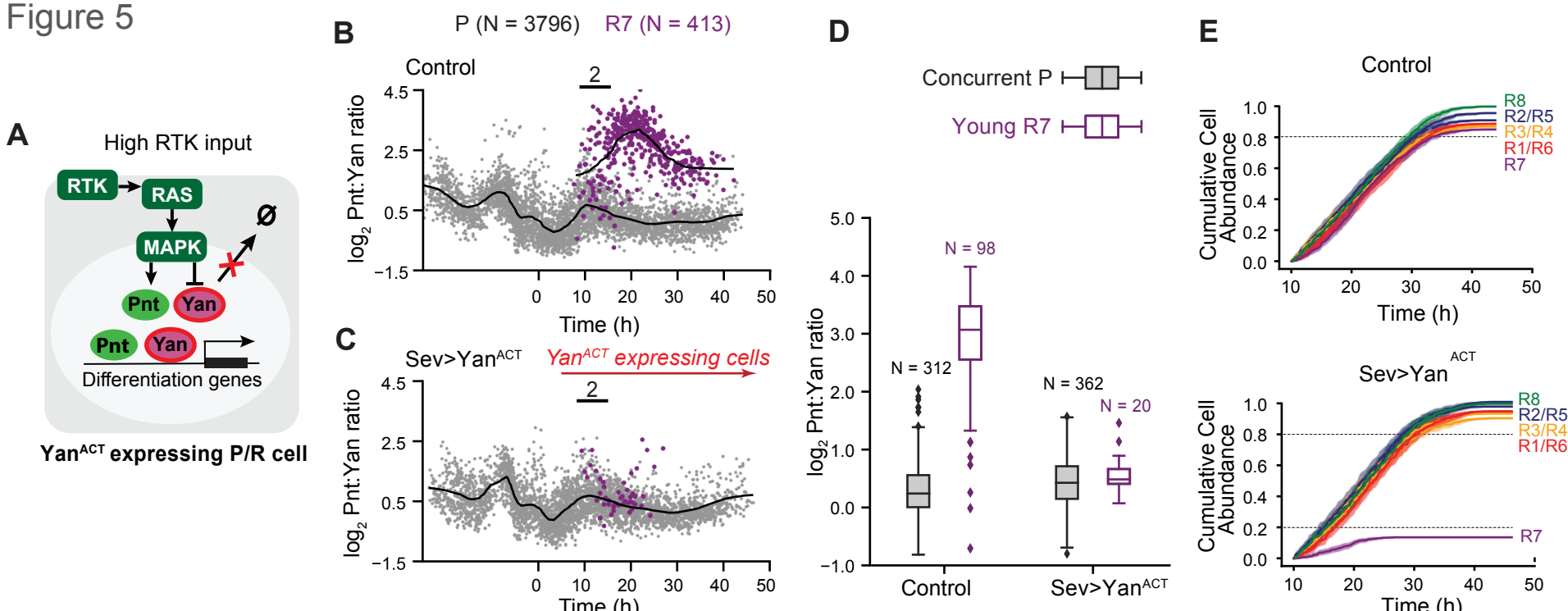
A
High RTK input
RTK
RAS
MAPK
Ø
Pnt
Yan
Pnt
Yan
Differentiation genes
YanACT expressing P/R cell
B
P (N = 3796)
R7 (N = 413)
Control
2
log2 Pnt:Yan ratio
Time (h)
C
Sev>YanACT
YanACT expressing cells
2
log2 Pnt:Yan ratio
Time (h)
D
Concurrent P
Young R7
N = 98
N = 312
N = 362
N = 20
log2 Pnt:Yan ratio
Control
Sev>YanACT
E
Control
Cumulative Cell Abundance
R8
R2/R5
R3/R4
R1/R6
R7
Time (h)
Sev>YanACT
Cumulative Cell Abundance
R8
R2/R5
R3/R4
R1/R6
R7
Time (h)

Figure 6

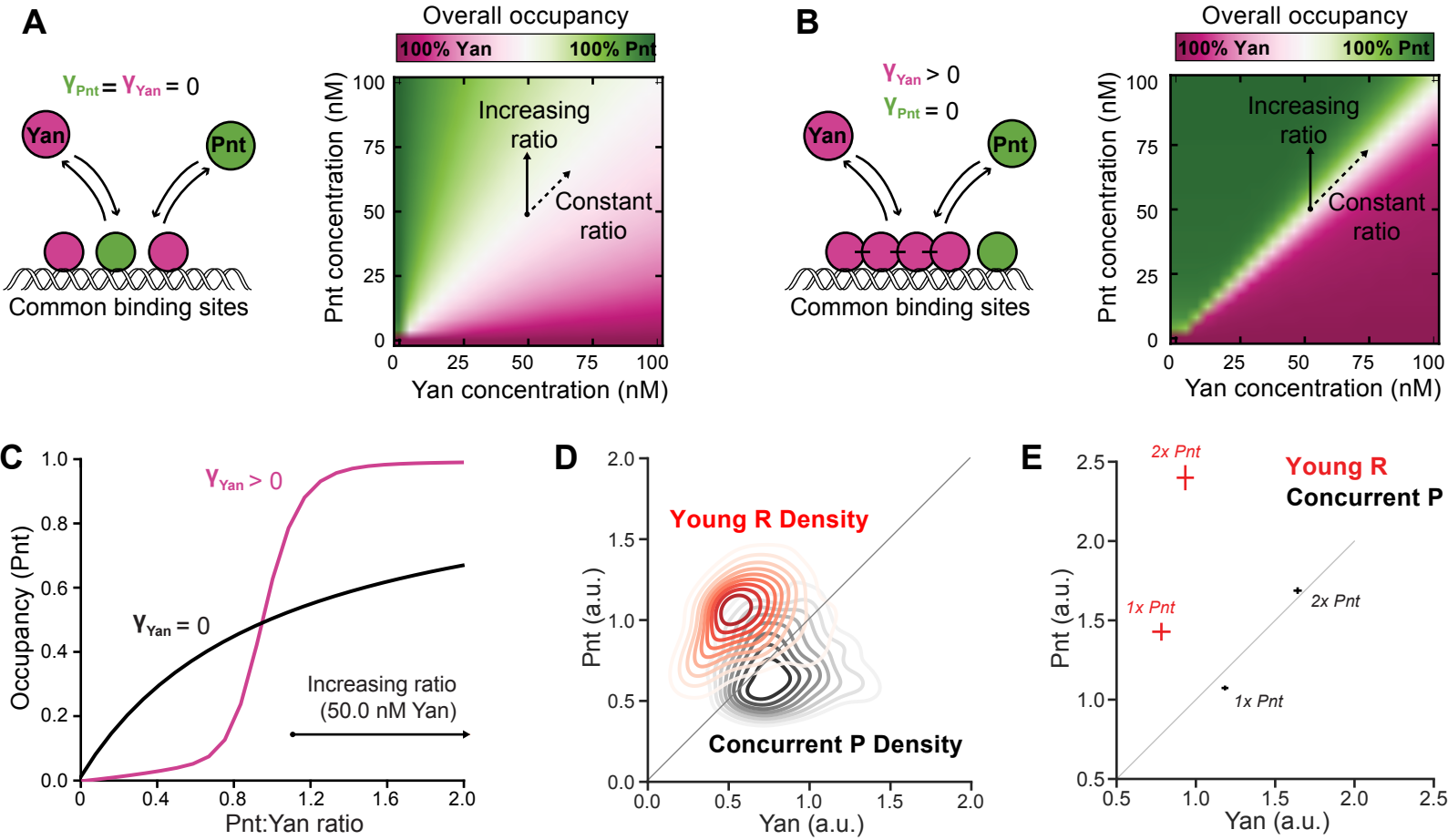
A
$\gamma_{Pnt} = \gamma_{Yan} = 0$
Yan
Pnt
Common binding sites
Overall occupancy
100% Yan
100% Pnt
Increasing ratio
Constant ratio
Pnt concentration (nM)
Yan concentration (nM)
B
$\gamma_{Yan} > 0$
$\gamma_{Pnt} = 0$
Yan
Pnt
Common binding sites
Overall occupancy
100% Yan
100% Pnt
Increasing ratio
Constant ratio
Pnt concentration (nM)
Yan concentration (nM)
C
$\gamma_{Yan} > 0$
$\gamma_{Yan} = 0$
Increasing ratio (50.0 nM Yan)
Occupancy (Pnt)
Pnt:Yan ratio
D
Young R Density
Concurrent P Density
Pnt (a.u.)
Yan (a.u.)
E
2x Pnt
1x Pnt
Young R
Concurrent P
2x Pnt
1x Pnt
Pnt (a.u.)
Yan (a.u.)

Table S1

Table S1. Accuracy of cell-type identification

Cell Type Scored	Cell Type Marker	Sample Size (*n*)	% Correct Type Assignment
Progenitors	Elav (-)	462	99.8
All mature Rs	Elav (+)	258	99.2
R8	Sens	106	97.2
R2/R5	Rough	162	99.4
R3/R4	Rough	142	100.0
R7	Pros	104	99.0

Figure S1

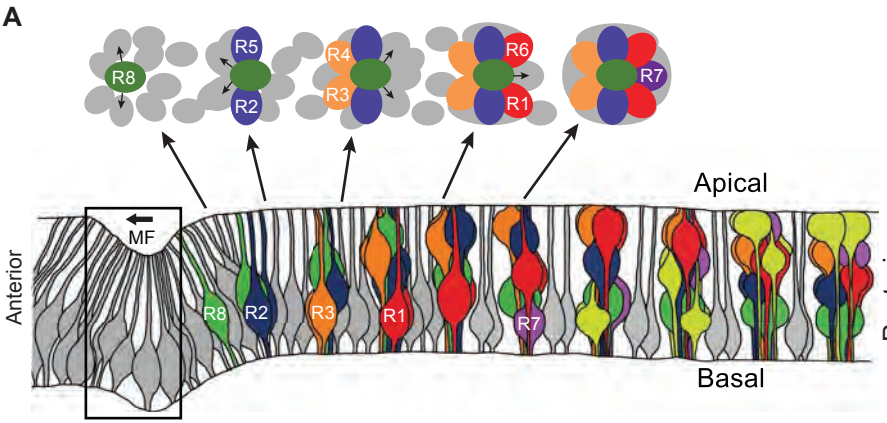
A
R8
R5
R2
R4
R3
R6
R1
R7
Apical
Basal
MF
Anterior
Posterior
R8
R2
R3
R1
R7

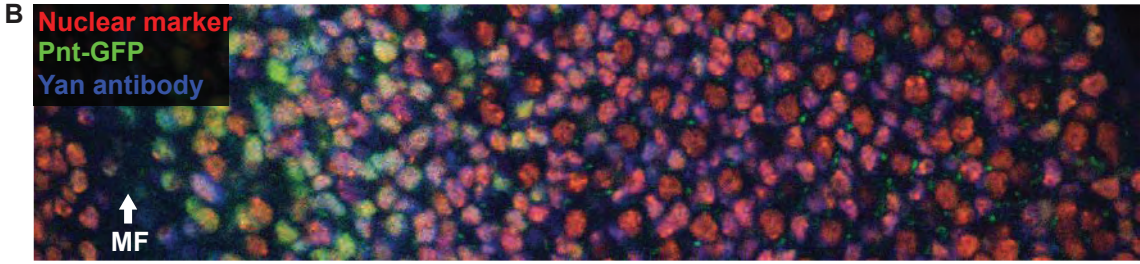
B
Nuclear marker
Pnt-GFP
Yan antibody
MF

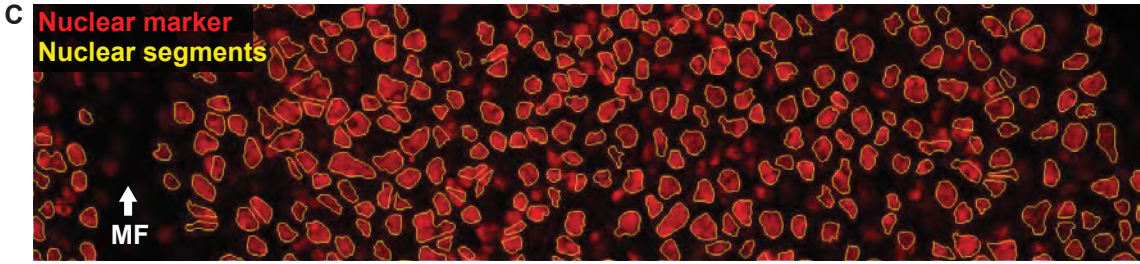
C
Nuclear marker
Nuclear segments
MF

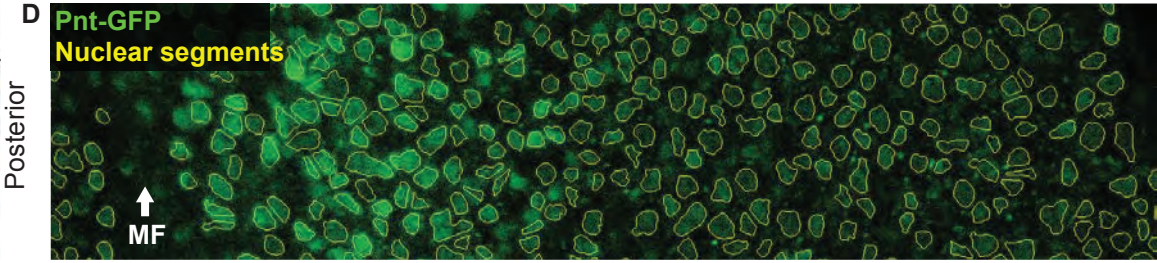
D
Pnt-GFP
Nuclear segments
MF

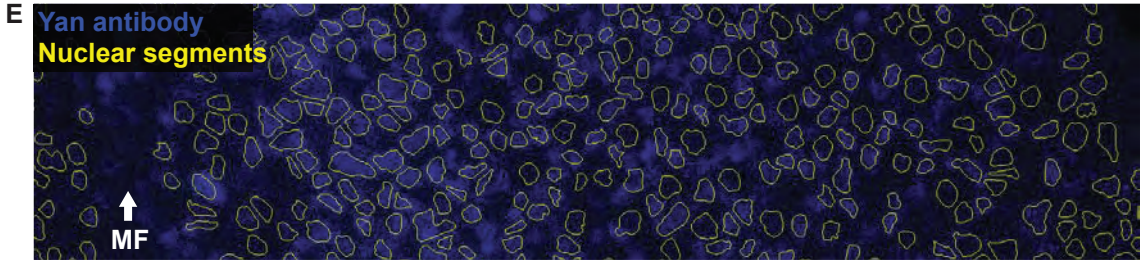
E
Yan antibody
Nuclear segments
MF

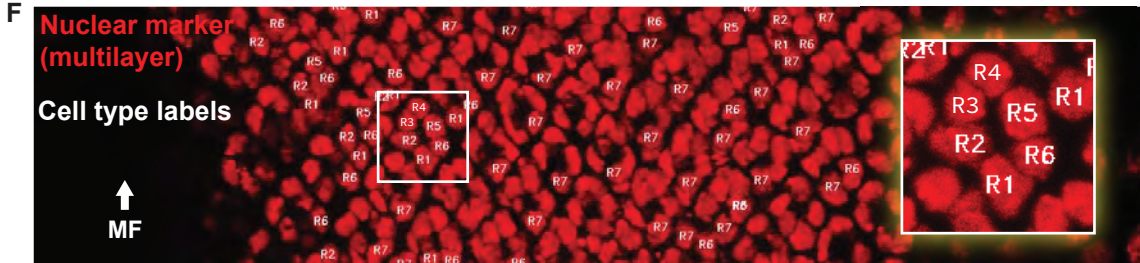
F
Nuclear marker
(multilayer)
Cell type labels
MF
R4
R3
R5
R1
R2
R6
R1

Figure S2

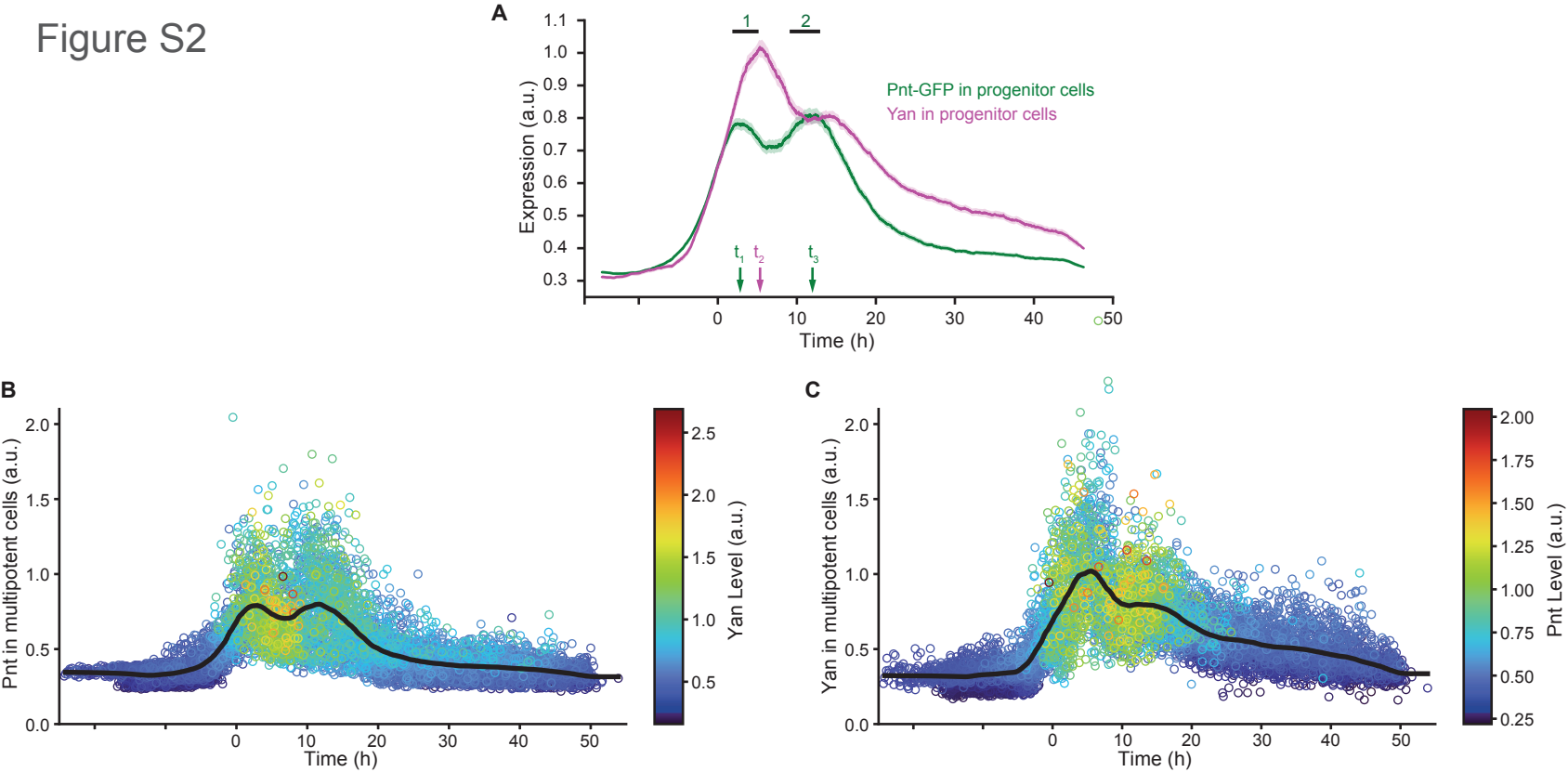
A
1
2
Pnt-GFP in progenitor cells
Yan in progenitor cells
Expression (a.u.)
Time (h)
B
Pnt in multipotent cells (a.u.)
Time (h)
Yan Level (a.u.)
C
Yan in multipotent cells (a.u.)
Time (h)
Pnt Level (a.u.)

Figure S3

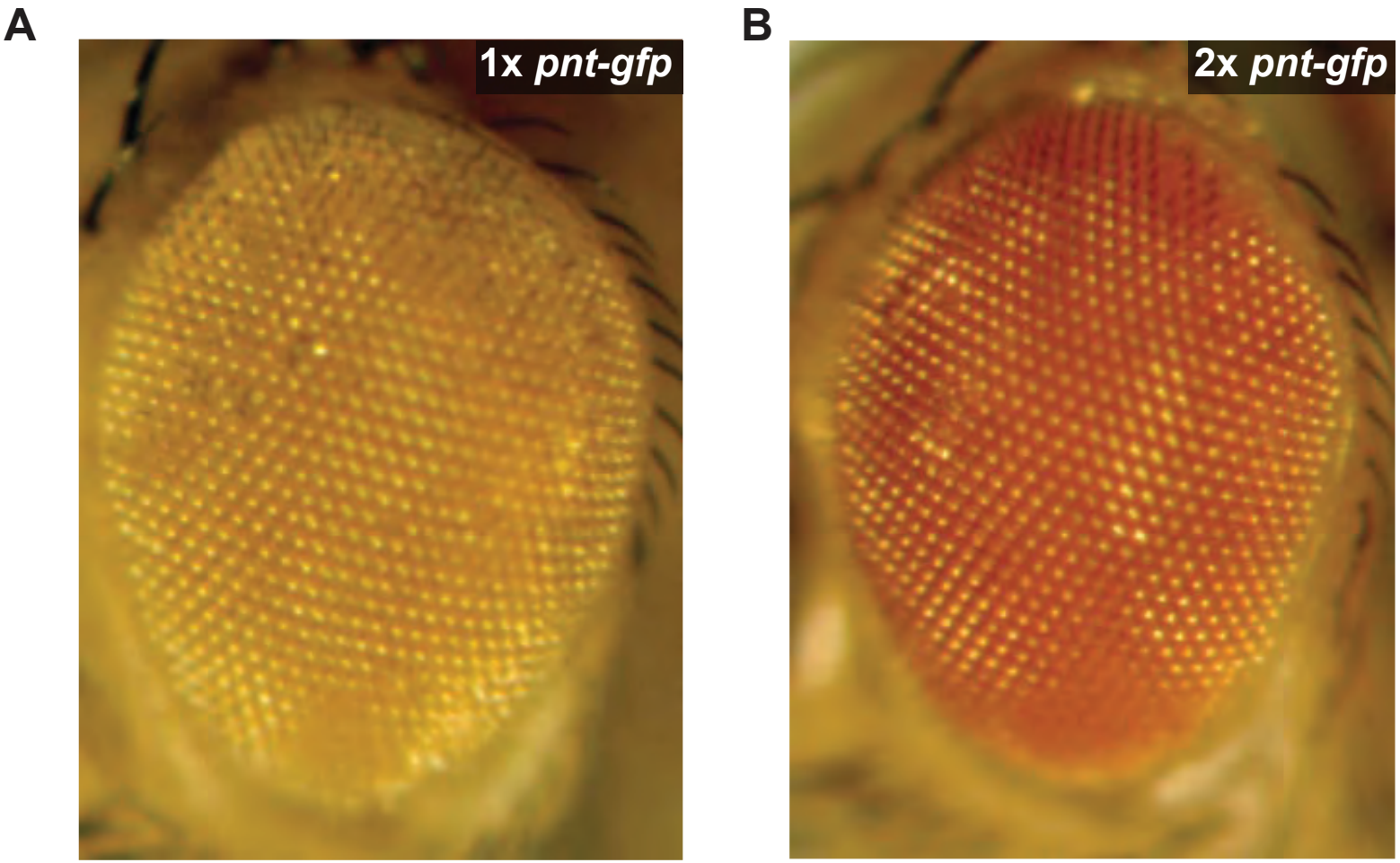

Figure S4

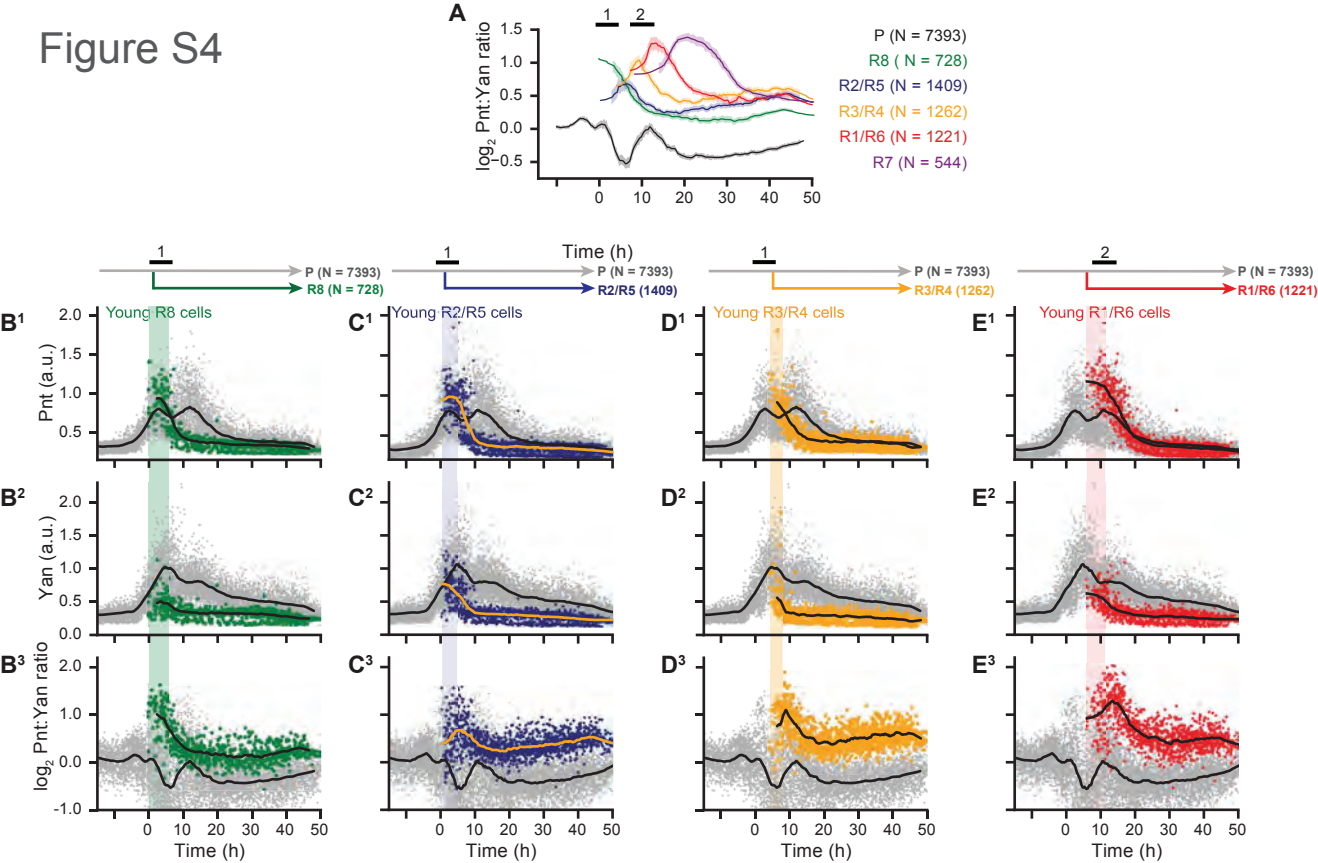
A
1
2
log2 Pnt:Yan ratio
1.5
1.0
0.5
0.0
−0.5
0
10
20
30
40
50
P (N = 7393)
R8 (N = 728)
R2/R5 (N = 1409)
R3/R4 (N = 1262)
R1/R6 (N = 1221)
R7 (N = 544)
Time (h)
P (N = 7393)
R8 (N = 728)
R2/R5 (1409)
R3/R4 (1262)
R1/R6 (1221)
B1
Young R8 cells
C1
Young R2/R5 cells
D1
Young R3/R4 cells
E1
Young R1/R6 cells
Pnt (a.u.)
B2
C2
D2
E2
Yan (a.u.)
B3
C3
D3
E3
log2 Pnt:Yan ratio
2.0
1.5
1.0
0.5
0.0
−1.0
Time (h)

Figure S5

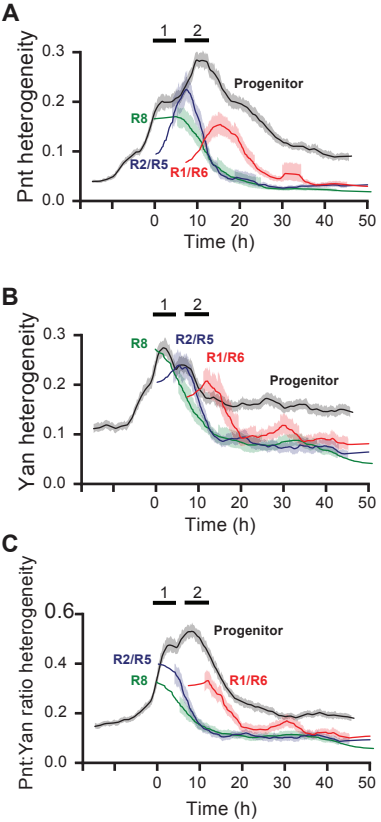
A
Pnt heterogeneity
0.3
0.2
0.1
0.0
1
2
Progenitor
R8
R2/R5
R1/R6
0
10
20
30
40
50
Time (h)
B
Yan heterogeneity
0.3
0.2
0.1
0.0
1
2
R8
R2/R5
R1/R6
Progenitor
0
10
20
30
40
50
Time (h)
C
Pnt:Yan ratio heterogeneity
0.6
0.4
0.2
0.0
1
2
Progenitor
R2/R5
R8
R1/R6
0
10
20
30
40
50
Time (h)

Figure S6

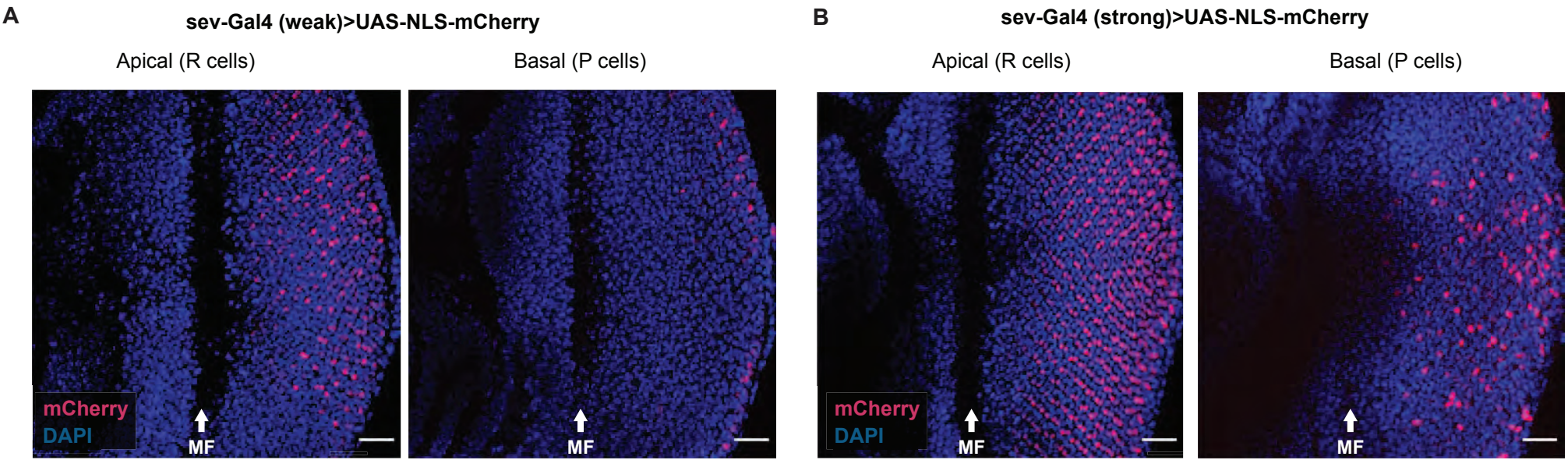
A
sev-Gal4 (weak)>UAS-NLS-mCherry
Apical (R cells)
Basal (P cells)
mCherry
DAPI
MF
MF
B
sev-Gal4 (strong)>UAS-NLS-mCherry
Apical (R cells)
Basal (P cells)
mCherry
DAPI
MF
MF

Figure S7

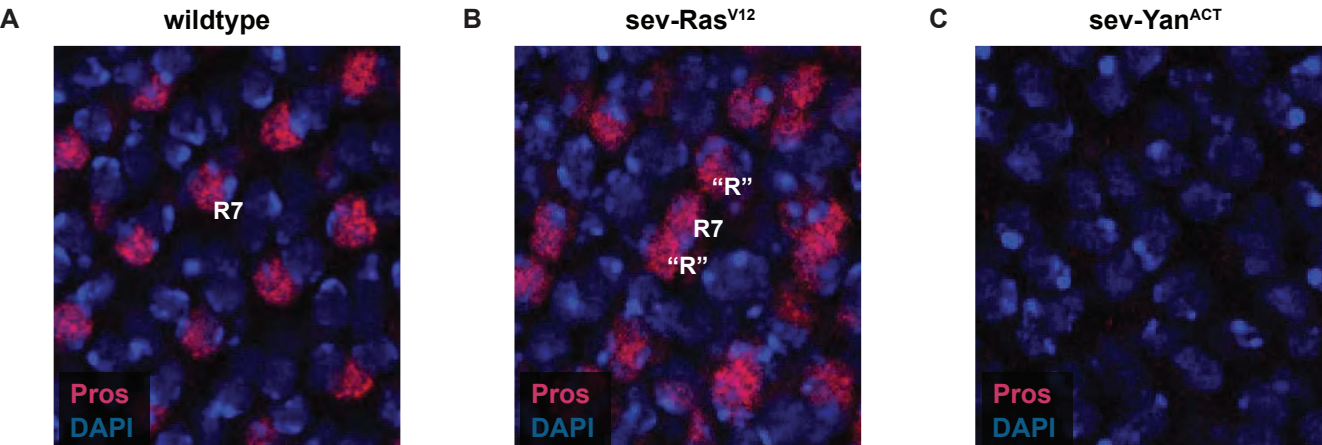
A
wildtype
R7
Pros
DAPI
B
sev-Ras^{V12}
"R"
R7
"R"
Pros
DAPI
C
sev-Yan^{ACT}
Pros
DAPI

Figure S8

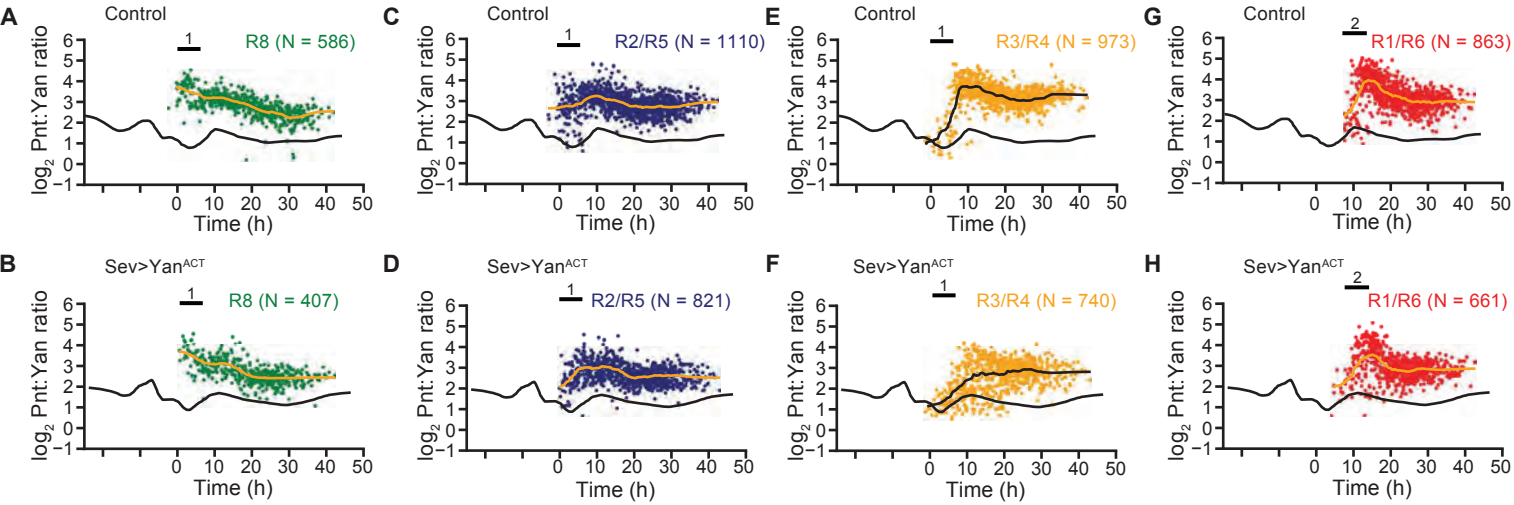
A
Control
R8 (N = 586)
B
Sev>Yan^ACT
R8 (N = 407)
C
Control
R2/R5 (N = 1110)
D
Sev>Yan^ACT
R2/R5 (N = 821)
E
Control
R3/R4 (N = 973)
F
Sev>Yan^ACT
R3/R4 (N = 740)
G
Control
R1/R6 (N = 863)
H
Sev>Yan^ACT
R1/R6 (N = 661)
log2 Pnt:Yan ratio
Time (h)

Figure S9

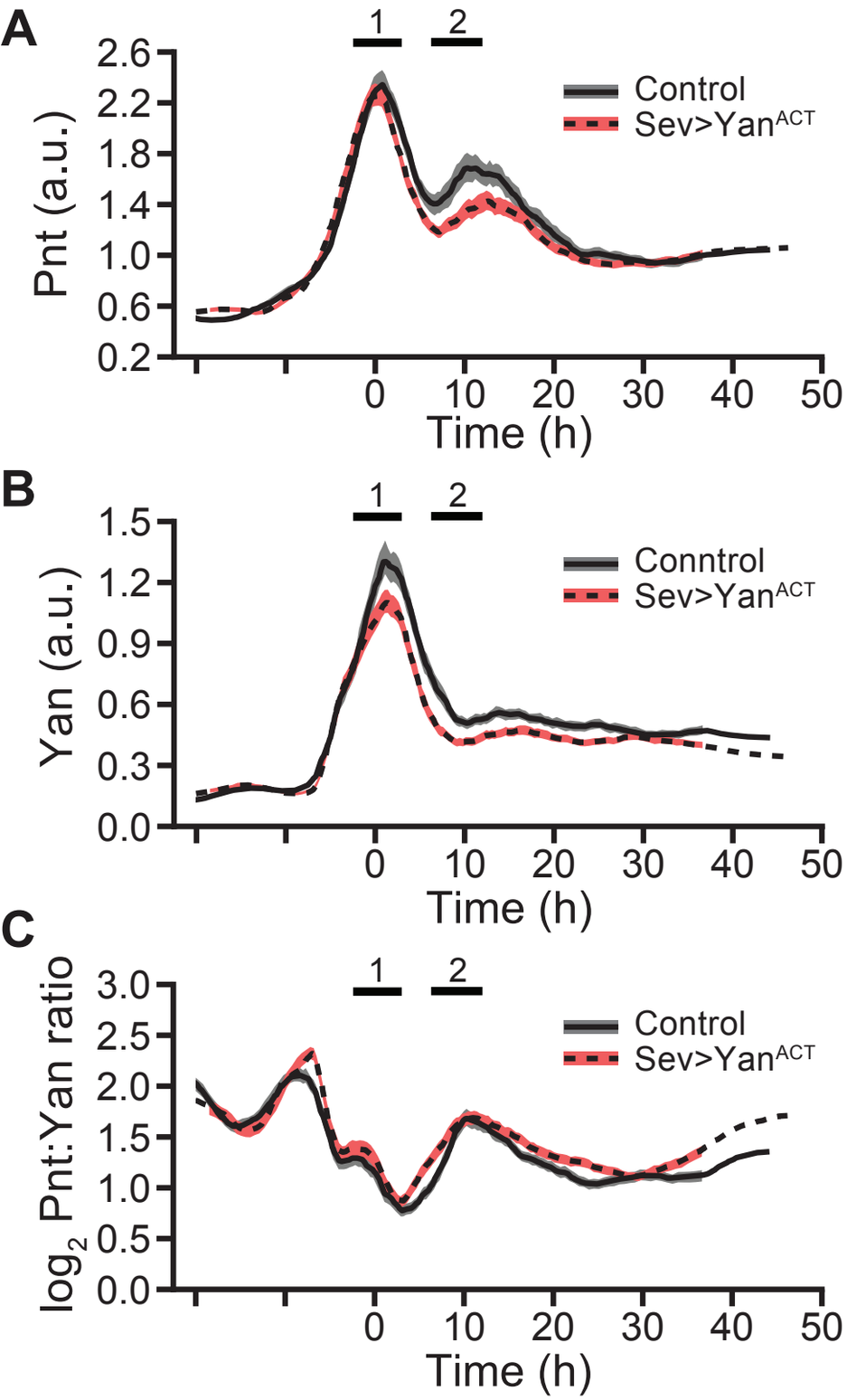
A
1
2
Control
Sev>Yan^ACT
Pnt (a.u.)
2.6
2.2
1.8
1.4
1.0
0.6
0.2
0
10
20
30
40
50
Time (h)
B
1
2
Conntrol
Sev>Yan^ACT
Yan (a.u.)
1.5
1.2
0.9
0.6
0.3
0.0
0
10
20
30
40
50
Time (h)
C
1
2
Control
Sev>Yan^ACT
log2 Pnt:Yan ratio
3.0
2.5
2.0
1.5
1.0
0.5
0.0
0
10
20
30
40
50
Time (h)

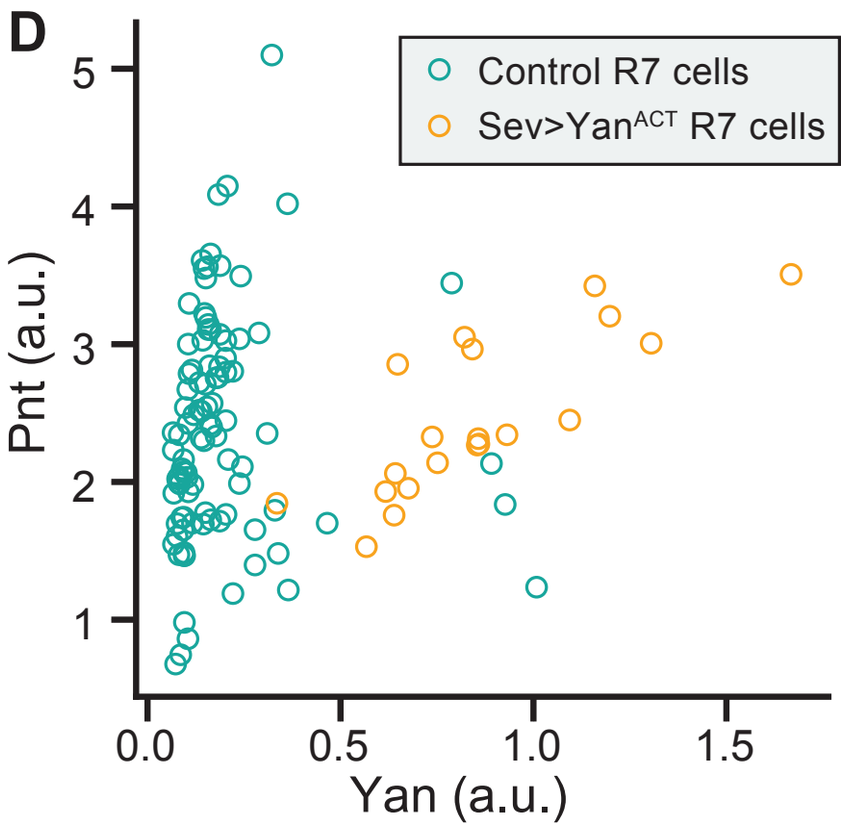
D
Control R7 cells
Sev>Yan^ACT R7 cells
Pnt (a.u.)
5
4
3
2
1
0.0
0.5
1.0
1.5
Yan (a.u.)

Figure S10

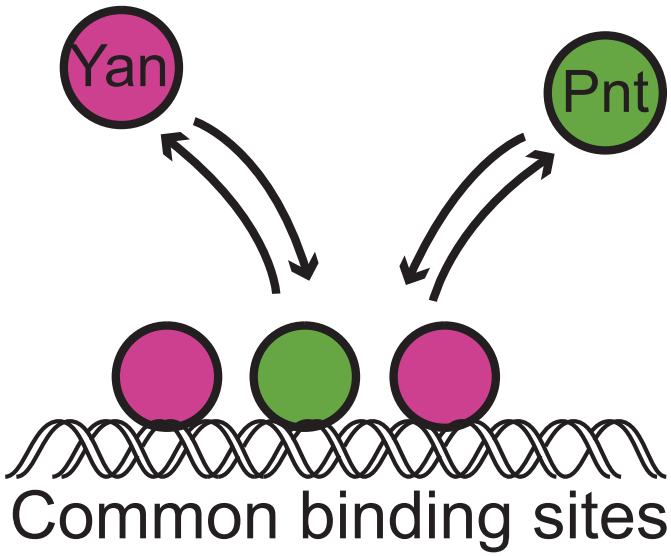
Yan
Pnt
Common binding sites

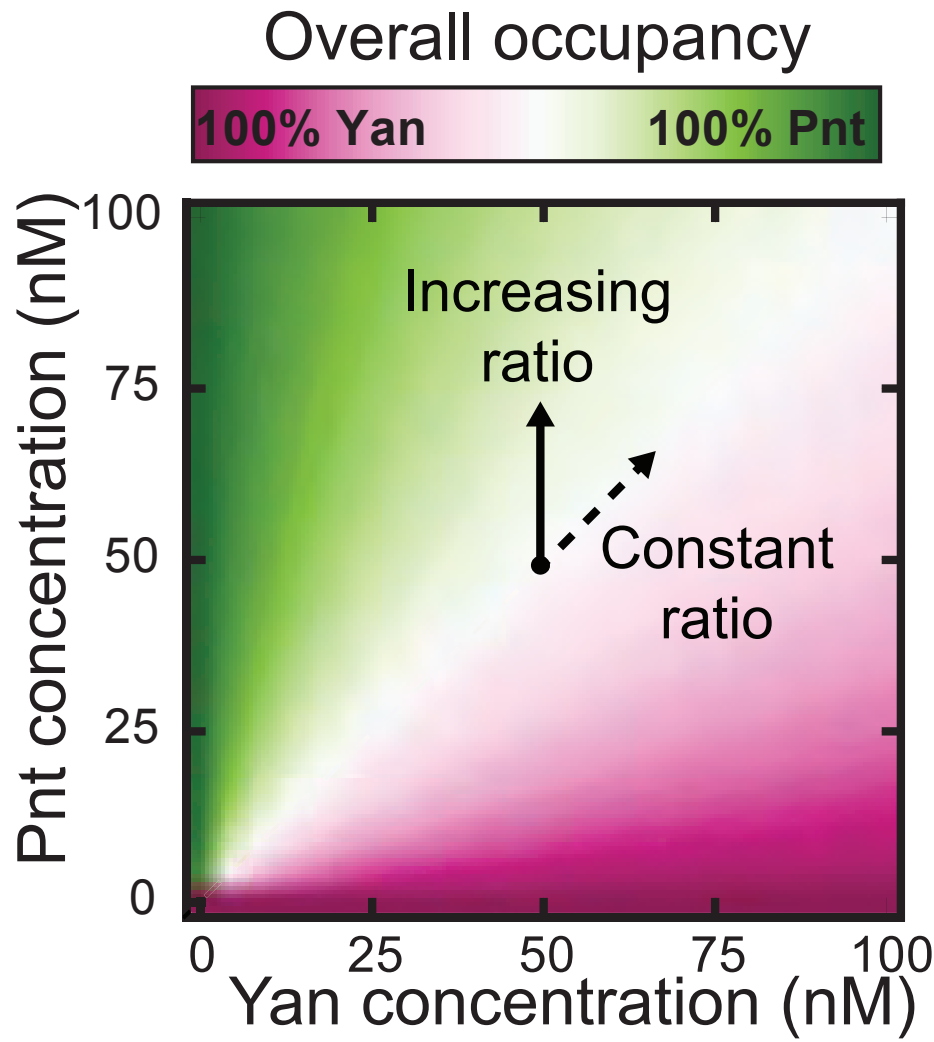
Overall occupancy
100% Yan
100% Pnt
Increasing ratio
Constant ratio
Pnt concentration (nM)
Yan concentration (nM)
0
25
50
75
100

Figure S11

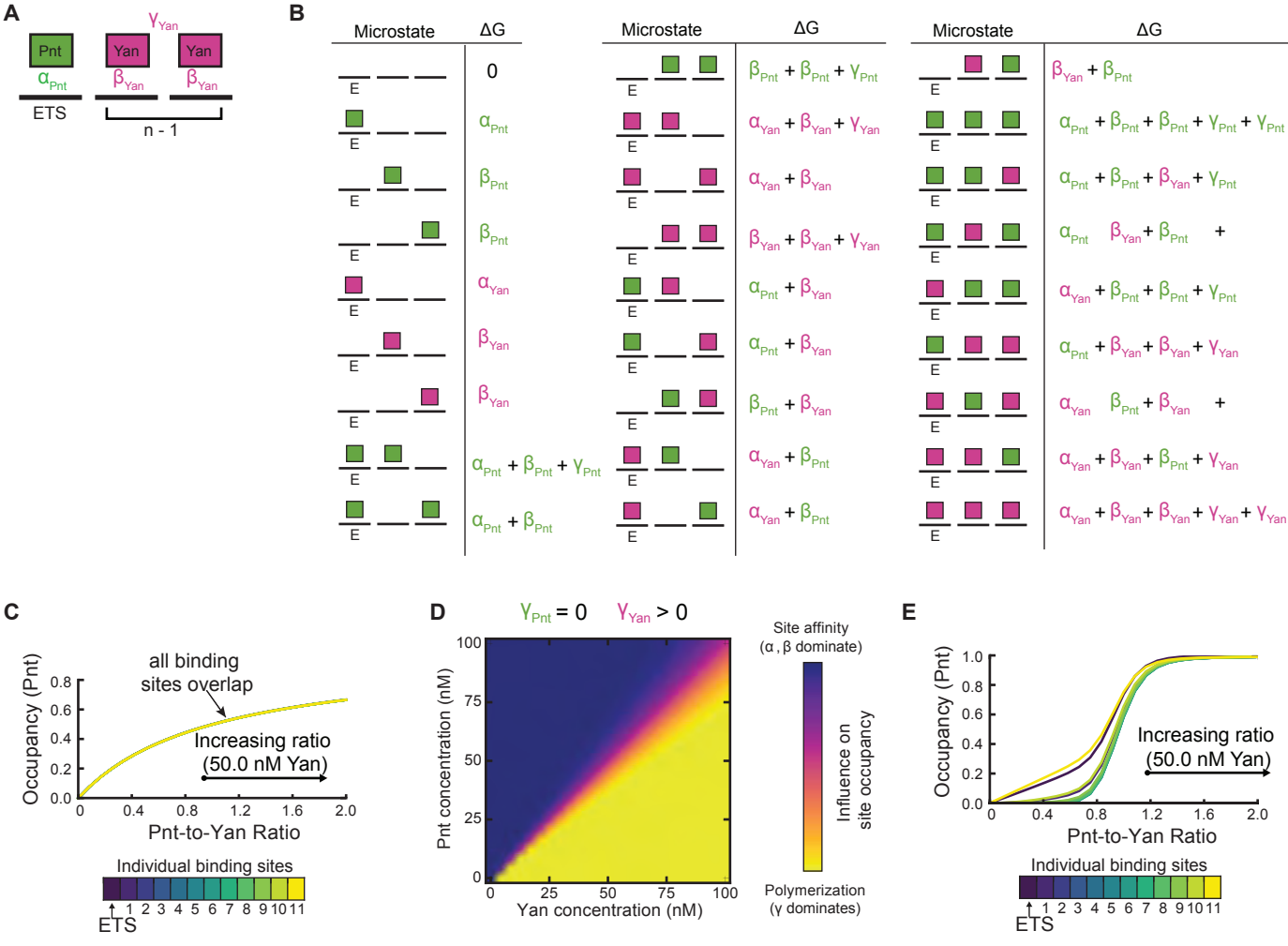
A
Pnt
Yan
Yan
γ_{Yan}
α_{Pnt}
β_{Yan}
β_{Yan}
ETS
n - 1
B
Microstate
ΔG
0
α_{Pnt}
β_{Pnt}
β_{Pnt}
α_{Yan}
β_{Yan}
β_{Yan}
$\alpha_{Pnt} + \beta_{Pnt} + \gamma_{Pnt}$
$\alpha_{Pnt} + \beta_{Pnt}$
$\beta_{Pnt} + \beta_{Pnt} + \gamma_{Pnt}$
$\alpha_{Yan} + \beta_{Yan} + \gamma_{Yan}$
$\alpha_{Yan} + \beta_{Yan}$
$\beta_{Yan} + \beta_{Yan} + \gamma_{Yan}$
$\alpha_{Pnt} + \beta_{Yan}$
$\alpha_{Pnt} + \beta_{Yan}$
$\beta_{Pnt} + \beta_{Yan}$
$\alpha_{Yan} + \beta_{Pnt}$
$\alpha_{Yan} + \beta_{Pnt}$
$\beta_{Yan} + \beta_{Pnt}$
$\alpha_{Pnt} + \beta_{Pnt} + \beta_{Pnt} + \gamma_{Pnt} + \gamma_{Pnt}$
$\alpha_{Pnt} + \beta_{Pnt} + \beta_{Yan} + \gamma_{Pnt}$
α_{Pnt} $\beta_{Yan} + \beta_{Pnt}$ +
$\alpha_{Yan} + \beta_{Pnt} + \beta_{Pnt} + \gamma_{Pnt}$
$\alpha_{Pnt} + \beta_{Yan} + \beta_{Yan} + \gamma_{Yan}$
α_{Yan} $\beta_{Pnt} + \beta_{Yan}$ +
$\alpha_{Yan} + \beta_{Yan} + \beta_{Pnt} + \gamma_{Yan}$
$\alpha_{Yan} + \beta_{Yan} + \beta_{Yan} + \gamma_{Yan} + \gamma_{Yan}$
E
C
Occupancy (Pnt)
all binding sites overlap
Increasing ratio (50.0 nM Yan)
Pnt-to-Yan Ratio
Individual binding sites
ETS
D
$\gamma_{Pnt} = 0$
$\gamma_{Yan} > 0$
Pnt concentration (nM)
Yan concentration (nM)
Site affinity (α , β dominate)
Influence on site occupancy
Polymerization (γ dominates)
E
Occupancy (Pnt)
Increasing ratio (50.0 nM Yan)
Pnt-to-Yan Ratio
Individual binding sites
ETS